



Published in final edited form as:

Neuron. 2020 July 08; 107(1): 52–64.e7. doi:10.1016/j.neuron.2020.04.003.

Molecular basis for synaptotagmin-1-associated neurodevelopmental disorder

Mazdak M. Bradberry^{1,2}, Nicholas A. Courtney¹, Matthew J. Dominguez³, Sydney M. Lofquist¹, Andrew T. Knox⁴, R. Bryan Sutton³, Edwin R. Chapman^{1,*,**}

¹Howard Hughes Medical Institute and Department of Neuroscience

²Medical Scientist Training Program, University of Wisconsin School of Medicine and Public Health, Madison, WI, 53705, USA

³Department of Cell Physiology and Molecular Biophysics, Texas Tech University Health Sciences Center, Lubbock, TX, 79430, USA; Center for Membrane Protein Research, Texas Tech University Health Sciences Center, Lubbock, TX, 79430, USA

⁴Department of Neurology, Section of Pediatric Neurology, University of Wisconsin School of Medicine and Public Health, Madison, WI, 53705, USA

SUMMARY:

At neuronal synapses, synaptotagmin-1 (syt1) acts as a Ca²⁺ sensor that synchronizes neurotransmitter release with Ca²⁺ influx during action potential firing. Heterozygous missense mutations in syt1 have recently been associated with a severe but heterogeneous developmental syndrome, termed syt1-associated neurodevelopmental disorder. Well-defined pathogenic mechanisms, and the basis for phenotypic heterogeneity in this disorder, remain unknown. Here, we report the clinical, physiological, and biophysical characterization of three syt1 mutations from human patients. Synaptic transmission was impaired in neurons expressing mutant variants, which demonstrated potent, graded dominant-negative effects. Biophysical interrogation of the mutant variants revealed novel mechanistic features concerning the cooperative action, and functional specialization, of the tandem Ca²⁺-sensing domains of syt1. These mechanistic studies led to the discovery that a clinically approved K⁺ channel antagonist is able to rescue the dominant-negative heterozygous phenotype. Our results establish a molecular cause, basis for phenotypic heterogeneity, and potential treatment approach for syt1-associated neurodevelopmental disorder.

eTOC blurb:

**Corresponding author; chapman@wisc.edu;

*Lead contact.

AUTHOR CONTRIBUTIONS

M.M.B. and E.R.C. conceived the project; M.M.B., N.A.C., S.L., M.J.D., and R.B.S. performed experiments and analysis; A.T.K. assisted with medical chart review; M.M.B., E.R.C., and A.T.K. wrote the paper; E.R.C. and R.B.S. supervised the work.

DECLARATION OF INTERESTS

The authors have no competing interests to declare.

Publisher's Disclaimer: This is a PDF file of an unedited manuscript that has been accepted for publication. As a service to our customers we are providing this early version of the manuscript. The manuscript will undergo copyediting, typesetting, and review of the resulting proof before it is published in its final form. Please note that during the production process errors may be discovered which could affect the content, and all legal disclaimers that apply to the journal pertain.

Bradberry et al. combine clinical, physiological, and biochemical approaches to define how mutations in the Ca^{2+} sensor synaptotagmin-1 lead to a severe neurodevelopmental disorder. Their studies define new mechanistic aspects of synaptotagmin-1's function and reveal that a clinically-approved drug may have a role in the treatment of this disorder.

INTRODUCTION

Synaptic transmission occurs via exocytosis of neurotransmitter-laden vesicles at nerve terminals. This membrane fusion process is catalyzed by soluble *N*-ethylmaleimide sensitive factor attachment protein receptors (SNAREs) (Sudhof and Rothman, 2009; Weber et al., 1998) and is rapidly triggered by an elevation in cytosolic Ca^{2+} ($[\text{Ca}^{2+}]_i$) that occurs upon the arrival of an action potential (Katz and Miledi, 1967). In most terminals, tandem-C2 domain proteins in the synaptotagmin (syt) family trigger SNARE-catalyzed membrane fusion via Ca^{2+} -dependent interactions with phospholipid bilayers (Bhalla et al., 2005; Mackler et al., 2002; Tucker, 2004). Synaptotagmin-1 (syt1), the predominant syt isoform in the central nervous system (CNS), likely acts by promoting vesicle docking (Chang et al., 2018; Liu et al., 2009; Reist et al., 1998), deforming the plasma membrane via Ca^{2+} -dependent membrane penetration by both C2 domains, C2A and C2B (Fig. 1A) (Bai et al., 2016; Evans et al., 2015; Hui et al., 2009; Liu et al., 2014), and potentially controlling the assembly of trans-SNARE complexes ((Bhalla et al., 2006; Kiessling et al., 2018; Zhou et al., 2015), but see also (Bai et al., 2016; Park et al., 2015)). Since each of these mechanistic findings continues to be the subject of debate, it is crucial to further address the precise biophysical action of syt1 in order to elucidate the molecular mechanisms that underlie excitation-secretion coupling (Brose et al., 2019).

Recently, a series of case reports has established a link between *de novo* heterozygous mutations in the gene encoding syt1 and a severe developmental syndrome (Baker et al., 2018, 2015). Patients with syt1-associated neurodevelopmental disorder demonstrate infantile hypotonia, profound intellectual disability, disordered movement, and electroencephalographic abnormalities without epilepsy or gross neuroanatomic abnormalities (Baker et al., 2018). The observed phenotypes vary widely in severity, but the basis for phenotypic heterogeneity in syt1-associated neurodevelopmental disorder is not well-defined. Previous studies indicate that other point mutations in syt1 can have dominant-negative effects in *Drosophila* (Mackler et al., 2002) and in cultured mouse neurons (Wu et al., 2017). While existing work suggests the disease-associated mutant variants described here may have a graded impact on synaptic vesicle recycling (Baker et al., 2018, 2015), whether and how these variants exert dominant-negative effects on synaptic transmission are key issues that require further exploration. Moreover, it remains unclear why all disease-associated mutations are clustered in the Ca^{2+} -binding, membrane-penetrating loops of C2B versus those of C2A.

In the present study, we establish a molecular basis for syt1-associated neurodevelopmental disorder by showing that these mutant variants impair the function of syt1 in a dominant-negative, but also graded, manner. We extend these findings to define key mechanistic insights into the action of syt1, and we provide a plausible basis for pharmacotherapy of

syt1-associated neurodevelopmental disorder using a clinically approved, centrally acting K⁺ channel antagonist.

RESULTS

Clinical manifestations of pathogenic syt1 mutations

Table 1 summarizes three exemplary cases of syt1-associated neurodevelopmental disorder. Clinical histories for each patient with a mutant variant were obtained from published studies (I368T) (Baker et al., 2015) or clinical records and interviews with parents (D304G, D366E). Detailed clinical histories for patients D304G and D366E are reported in STAR methods. In each case, heterozygous *de novo* mutations in *SYT1* were discovered by whole-exome sequencing, which excluded a causal role for inherited mutations (STAR methods). Mutations for patients D366E and I368T were confirmed by Sanger sequencing (Fig. S1). As noted in the case series by Baker et al (2018), these mutations are associated with a profound global developmental delay that varies widely in severity. All patients exhibited hypotonia and delayed motor development apparent in the first year of life. As with patient I368T, magnetic resonance imaging of the brains of patients D304G and D366E revealed no gross neuroanatomical abnormalities, and extensive testing in each patient did not reveal any underlying metabolic abnormalities (STAR methods). Developmental regression and seizures were absent in all cases, but electroencephalogram (EEG) revealed background slowing and intermittent high-amplitude, low-frequency spiking activity in each case. Strikingly, the EEG disturbance was also graded, and the amplitude of spiking activity correlated with the severity of developmental delay (i.e., I368T > D366E). Two of these patients, D366E and I368T, underwent visual evoked potential recording, which demonstrated abnormally prolonged latency in both cases. Behavioral phenotypes also varied in type and severity, with two of these patients (D304G and I368T) exhibiting frequent agitation and self-injurious behavior. These cases highlight the phenotypic variability of syt1-associated neurodevelopmental disorder, with patient D366E demonstrating a substantially milder global phenotype than patients D304G and I368T. We note that the variants described here represent only a subset of disease-associated syt1 mutations, as two additional variants (M303K, N371K) have also been reported (Baker et al., 2018).

Crystal structures of syt1 C2B domains harboring pathogenic mutations

We first undertook a structural analysis to define the molecular phenotype associated with these three mutations, all of which occur in the cytoplasmic C2B domain of this tandem-C2 domain protein (Figure 1A). X-ray crystallographic structures of each mutant variant C2B are shown in Fig. 1B, and the Ca²⁺-binding regions for each domain are shown in Fig. 1C. Ca²⁺-free conditions were chosen to facilitate crystallization and because the conformational changes that occur upon Ca²⁺ binding are minimal (Shao et al., 1998). Compared with the wild-type domain, each mutant variant C2B is correctly folded in the β -sandwich of a C2 domain (Fig. 1B). While subtle differences in the position of Ca²⁺-binding/membrane-penetration loops were apparent (Fig. 1C), these residues are likely to be highly mobile in solution, and the observed differences are likely attributable to differences in crystal packing. Fig. 1 also highlights the physicochemical diversity of these mutations. D304G

neutralizes a Ca²⁺-binding aspartic acid, while D366E preserves a carboxylate ligand but reduces the size of the Ca²⁺-binding pocket (Fig. 1C). I368T substitutes a polar threonine for a bulky, hydrophobic isoleucine that normally penetrates the plasma membrane upon Ca²⁺ binding by syt1 (Bai et al., 2002). As other authors have emphasized (Baker et al., 2018), the affected residues are highly conserved in syt1 homologs across the metazoan phylogeny.

Disease-associated syt1 variants traffic normally but fail to support synaptic transmission

As noted above, each disease-associated mutation occurs at a residue with a defined biochemical function in the loops of C2B (Chang et al., 2018; Evans et al., 2015; Hui et al., 2009). However, studies of synaptic transmission in neurons expressing syt1 with C2B loop mutations have only rarely examined single point mutations, and mutations at some of these sites appear inconsequential (Mackler et al., 2002; Nishiki and Augustine, 2004). Because limited evidence points to deficits in vesicular recycling of disease-associated syt1 variants (Baker et al., 2018), we assessed the trafficking and synaptic function of each variant using immunocytochemistry and electrophysiological recordings of synaptic currents in cultured mouse hippocampal and cortical neurons (Fig. 2; please note: in these and all subsequent experiments, amino acid numbers for the rat and mouse syt1 sequences are used). Using a specific antibody against syt1 (Fig. S2), we found that each mutant variant trafficked as effectively as WT to the presynaptic compartment (Fig. 2A-B). We note that, while each of these variants trafficked normally and was thus assessed for synaptic function, other disease-associated mutations may act by causing mislocalization of syt1 (Baker et al., 2018).

We next measured evoked GABAergic postsynaptic currents (IPSCs) from WT or syt1 KO cortical neurons expressing mutant syt1 variants (Fig. 2C). Despite localizing correctly to presynaptic terminals, mutant syt1 variants largely failed to support evoked synaptic transmission (Fig. 2D-G). However, this effect was graded: while the evoked-transmission phenotypes of D303G and I367T appeared nearly identical to the syt1 KO (Fig. 2D-G), D365E preserved the rapid kinetics of wild-type syt1 (Fig. 2E,H), despite also exhibiting the low amplitude and total charge transfer properties of the KO (Fig. 2F-G).

Syt1 also regulates spontaneous neurotransmitter release by suppressing, or clamping, fusion under resting conditions (Courtney et al., 2019; Liu et al., 2009). We observed that clamping of spontaneous vesicle fusion, as represented by the frequency of miniature IPSCs (mIPSCs), also varied among the genotypes: variants I367T and D365E clamped mIPSCs more effectively than D303G (Fig. 2I), consistent with an established but poorly-understood role for Ca²⁺-binding loops in the clamping action of syt1 (Evans et al., 2015; Lee et al., 2013). In summary, the pathogenic syt1 mutations affect spontaneous release rates and strongly impact evoked release. Importantly, and in correlation with the observed clinical phenotypes, D303G and I367T cause an even more severe impairment of evoked synaptic release than D365E.

Disease-associated syt1 variants exhibit a graded dominant-negative impact on neurotransmitter release

We next assessed the dominant-negative potency of each mutation with simultaneous lentiviral expression of mutant and WT syt1, in combination with optical imaging of evoked

glutamate release (Fig. 3) (Marvin et al., 2013). Hippocampal neurons cultured from *Syt1^{fl/fl}* mice were transduced with lentivirus encoding Cre recombinase along with separate lentiviruses encoding WT and mutant syt1, respectively (Fig. 3A-B). In each experiment the WT and mutant syt1 expression levels obtained using each dose of lentivirus were measured in separate, parallel samples by immunoblot analysis (Fig 3A-B). A range of WT:mutant expression ratios was assessed, and evoked glutamate release was measured as the normalized change in fluorescence across a field of view in response to a 10-AP, 10-Hz field stimulus (Fig. 3C-H). iGluSnFR fluorescence transient amplitudes were plotted against the relative expression of WT and mutant protein in Fig. 3E, clearly demonstrating a dominant-negative action of each mutant syt1 variant. Even at sub-stoichiometric expression levels, mutant variants dose-dependently inhibited action-potential-evoked glutamate release (Fig. 3E). Strikingly, and in accordance with the findings of Baker et al. (2018), we observed a graded dominant-negative potency (D303G \approx I367T > D365E) that again correlated with the observed clinical phenotypes (Fig. 3E-F). Comparison of iGluSnFR data from all samples demonstrated a similar effect even without controlling for expression level (Fig. S3), and statistical tests supported the use of separate lines to fit the data for each mutant (Table S2). We obtained nearly identical results recording GABAergic IPSCs from neurons transduced with lentivirus to target equal expression of WT and mutant variants (Fig. S4), though the effect of coexpressing variant D365E did not reach statistical significance in those experiments. As a relative measure of synaptic release probability, we also measured the amplitude of the tenth iGluSnFR transient normalized to that of the first transient ($dF/F_0(\text{tenth/first})$) (Fig. 3G-H). As expected, $dF/F_0(\text{tenth/first})$ increased with the expression of mutant protein, indicating a dose-dependent reduction in relative release probability (Fig. 3G). As with the amplitude of the first response, mutant syt1 variants exhibited graded, dominant-negative activity, with D365E expressing the mildest phenotype (Fig. 3G-H). Together, these results unambiguously establish the dominant-negative action of each mutant variant and strongly suggest a physiologic basis for the phenotypic heterogeneity observed in these patients.

Disease-associated syt1 variants show impaired binding to Ca^{2+} and lipids

Syt1 triggers SNARE-catalyzed membrane fusion *in vitro* and at neuronal synapses by Ca^{2+} -dependent membrane insertion of residues in two flexible loops in both C2A and C2B (Bai et al., 2016; Courtney et al., 2019; Evans et al., 2015; Liu et al., 2014; Tucker, 2004). This interaction requires negatively-charged phospholipids, namely phosphatidylserine (PS) and/or phosphatidylinositol(4,5)-bisphosphate (PIP_2) (Wang et al., 2011). PIP_2 , in particular, is a dynamically-regulated phospholipid (Micheva et al., 2001) that plays an important role in exocytosis (Eberhard et al., 1990). Importantly, syt1 can bind and partially penetrate PIP_2 -containing membranes even in the absence of Ca^{2+} , allowing for enhanced kinetics of Ca^{2+} -dependent membrane penetration (Bai et al., 2004; Bradberry et al., 2019).

We thus performed a series of studies with purified protein and liposomes to define how mutant syt1 variants interact with Ca^{2+} and membranes (Fig. 4). In saturating $[\text{Ca}^{2+}]_{\text{free}}$ (1 mM), the purified tandem C2 domains (C2AB) of each syt1 variant displayed largely intact Ca^{2+} -dependent and -independent binding to phospholipid bilayers containing PS with or without PIP_2 (Fig. 4A-C). However, each mutant variant showed diminished binding to

Author Manuscript

bilayers containing PIP₂ as the sole acidic phospholipid, consistent with an established role for C2B as the primary PIP₂-binding domain of syt1 (Fig. 4A-C) (Bai et al., 2004). A detailed titration of [Ca²⁺]_{free} in the presence of PS:PIP₂ vesicles demonstrated a substantial reduction in the Ca²⁺-sensitivity of membrane binding for each mutant variant (Fig. 4D-E). This effect was graded in a fashion that correlated with the severity of both the synaptic and human phenotypes for each mutation (Fig. 4E). In particular, at 10 μM Ca²⁺, a relevant Ca²⁺ concentration at release sites during action potential firing in cultured hippocampal neurons (Burgalossi et al., 2010), D365E exhibited substantially more Ca²⁺-dependent binding than either D303G or I367T (Fig. 4E). In general, the Ca²⁺ cooperativity of membrane binding was low for WT and mutant variants (Hill coefficients ± standard error: WT, 1.6 ± 0.2; D303G, 1.4 ± 0.2; D365E, 1.1 ± 0.1; I367T, 2.1 ± 0.4). t-SNARE binding activity, by comparison, was unaffected by each mutation in both the presence and absence of saturating [Ca²⁺]_{free} (Fig. S5).

Author Manuscript

To assess the stability of the syt1 C2AB-Ca²⁺-phospholipid complex formed by WT and mutant protein, we performed a time-resolved assay to measure the kinetics of Ca²⁺ release from these complexes (Fig. 4F-H) (Nalefski et al., 2001). In this assay, the fluorescent Ca²⁺ chelator quin-2 is rapidly mixed with pre-assembled C2AB-Ca²⁺-phospholipid complexes in a stopped-flow fluorescence spectrometer, and observable kinetic information corresponds to liberation of Ca²⁺ from the protein-lipid complex (Fig. S6). We observed that Ca²⁺ release was more rapid in complexes containing mutant C2AB (Fig. 4G-H). Fitting of double exponential decay functions to the observed data revealed a fast and a slow component for each trace (Fig. 4H). WT protein exhibited a more predominant slow component of Ca²⁺ release (Fig. 4H), indicating that in the activated, membrane-bound state, WT syt1 forms more stable complexes with Ca²⁺ as compared to the three mutant proteins.

Author Manuscript

Disease-associated mutations impair distinct membrane penetration modes in C2A and C2B

Thus far, all disease-causing syt1 mutations occur in the C2B domain of the protein (Baker et al., 2018), and a host of studies have found that syt1 is more functionally susceptible to mutations in C2B than in C2A (Chapman, 2008; Shin et al., 2009). However, the biophysical basis for this C2B-dependence remains unclear, as C2A has an equal number of Ca²⁺-binding residues and binds at least as many Ca²⁺ ions (Fernandez et al., 2001; Shao et al., 1998; Sutton et al., 1995). Moreover, studies using the individual C2 domains are difficult to meaningfully interpret, as significant evidence exists for a functional linkage between the two domains (Bai et al., 2002; Courtney et al., 2019; Evans et al., 2016; Herrick et al., 2006).

Author Manuscript

To better delineate the roles of C2A and C2B, we developed an assay to carefully assess membrane penetration by either domain in the context of the tandem domains (Fig. 5). Purified syt1 C2AB was first labeled at introduced cysteine residues with an environmentally sensitive probe, NBD, on a Ca²⁺-binding/membrane penetration loop in C2A (F234C-NBD) or C2B (V304C-NBD). This dye undergoes a blue shift and substantial emission intensity increase when buried in the hydrophobic core of the bilayer (Fig. 5B). Labeled syt1 was then combined with PIP₂-containing vesicles such that NBD-syt1 was

completely adsorbed to the surface of the liposomes even in the absence (<10 nM) of free Ca^{2+} (Fig. S7). Under these conditions, the Ca^{2+} -dependent membrane penetration activities of C2A and C2B can be examined independently, as avidity effects (i.e., apparent coupling of penetration by C2A and C2B due to an entropic benefit for one domain following binding by the other) are largely avoided.

Changes in NBD fluorescence, while titrating Ca^{2+} in samples containing WT or mutant syt1 C2AB, are depicted in Fig. 5B-C. Two key features emerge from these data: first, in WT syt1, C2B exhibited a substantially higher sensitivity to Ca^{2+} than C2A. Second, pathogenic mutations reduced the Ca^{2+} -sensitivity of membrane penetration by both C2A and C2B, though with a more pronounced effect on C2B (Fig. 5C-D). These results demonstrate that, in WT syt1, Ca^{2+} binds more tightly to C2B than C2A at the protein-membrane interface, implying that more free energy is liberated via Ca^{2+} -triggered penetration by C2B ($G = -RT \ln K_{eq}$). For each mutant variant, this high-affinity mode was abolished in a graded fashion, and the Ca^{2+} -dependence of membrane penetration by C2B more closely resembled that of C2A (Fig. 5C,D). As with our previous studies, D303G had the most potent effect on membrane penetration (Fig. 5B-C). D365E and I367T had similar $[\text{Ca}^{2+}]_{1/2}$ values, but as in our lipid-binding assays (Fig. 4E), D365E had relatively more activity at low $[\text{Ca}^{2+}]_{free}$ versus I367T (Fig. 5C). We also observed an apparent increase in the cooperativity of Ca^{2+} -dependent membrane penetration for some of the mutants versus the WT protein (Hill coefficients \pm SE: WT C2A, 1.0 ± 0.1 ; WT C2B, 0.8 ± 0.1 ; D303G C2A, 1.6 ± 0.2 ; D303G C2B, 1.6 ± 0.2 ; D365E C2A, 1.3 ± 0.2 ; D365E C2B, 1.4 ± 0.2 ; I367T C2A, 1.4 ± 0.2 ; I367T C2B, 1.9 ± 0.8). Variants D303G and D365E also caused a reduction in the Ca^{2+} sensitivity of penetration by C2A (Fig. 5D-E), consistent with reports of functional cooperativity between C2A and C2B when linked (Bai et al., 2002; Courtney et al., 2019; Evans et al., 2016; Herrick et al., 2006). Together, these data establish a biophysical basis for the functional dominance of syt1's C2B domain and, in turn, the presence of disease-causing mutations in the membrane penetration loops of C2B versus those of C2A (Fig. 5F).

Rescue of dominant-negative synaptic impairments by 4-aminopyridine

Even when a molecular cause is well-defined, treatment of inherited developmental disorders is a challenging prospect given the paucity of suitable gene therapies. However, depending on the consequences of a given mutation, rationally guided treatment may benefit some patients. Because each mutation described here reduces the Ca^{2+} sensitivity of membrane binding and penetration by syt1, boosting presynaptic Ca^{2+} influx might mitigate the synaptic deficits associated with each mutant. Indeed, Baker and colleagues (2018) were able to rescue the trafficking deficits of these mutant variants by increasing extracellular $[\text{Ca}^{2+}]$, though it is unclear how this might be achieved clinically.

We reasoned that pharmacologic approaches might also be used to enhance presynaptic Ca^{2+} influx. 4-aminopyridine (4-AP, fampridine, dalfampridine) (Fig. 6A) is a K^+ channel antagonist clinically approved for the treatment of multiple sclerosis (Leussink et al., 2018). This drug, which is selective for K_v3 channels at low concentrations (Alle et al., 2011), would be expected to broaden action potentials and thus enhance presynaptic Ca^{2+} influx.

Moreover, a non-centrally-acting variant of 4-AP, 3,4-diaminopyridine, has been used successfully to treat a myasthenic syndrome associated with similar mutations in synaptotagmin-2, the predominant syt isoform at the neuromuscular junction (Whittaker et al., 2015). In neurons transduced to express roughly equal amounts of mutant and WT syt1, 4-AP dose-dependently enhanced evoked glutamate release and restored normal short-term plasticity (Fig. 6B-D). At 5 μ M, the dominant-negative effects of each mutant on the amplitude of the first glutamate transient (Fig. 6C), as well as dF/F_0 (tenth/first) (Fig. 6D), were largely mitigated, and responses appeared similar to those of WT neurons in the absence of drug. We emphasize that additional considerations apply in the clinical setting, particularly given the convulsant effects of higher doses of 4-AP. However, these results—particularly given the lack of epilepsy in patients with syt1 mutations—suggest that 4-AP or other centrally-acting K_v channel blockade presents a plausible approach to pharmacotherapy for these patients.

DISCUSSION

Causative mechanisms in syt1-associated neurodevelopmental disorder

Each mutation studied here selectively alters the physicochemical properties of the Ca^{2+} -binding, membrane-penetrating loops of syt1 C2B (Fig. 1), with dramatic and deleterious consequences for synaptic transmission (Fig. 2). Even the most conservative mutation, D366E, caused near-complete loss of function in syt1 despite previous studies suggesting that a neutralizing mutation (D>N) at this position should have only mild effects (Nishiki and Augustine, 2004). Our results demonstrate that the Ca^{2+} -binding pocket of syt1 C2B is exquisitely tuned, highlighting the difficulty of predicting a mutation's functional impact based on biochemical principles alone. Moreover, our observations strongly suggest that these mutant syt1 variants likely provide little support for synaptic transmission *in vivo*, supporting a role for these mutations in the observed clinical phenotypes.

An unambiguous causal role for these mutations, however, requires a capacity for mutant syt1 to act in a dominant-negative manner. Previous studies have suggested that human syt1 mutant variants undergo impaired vesicular recycling (Baker et al., 2018), and unrelated heterozygous mutations in *Drosophila* syt1 have been shown to impair neurotransmitter release (Mackler et al., 2002). The current study, by contrast, is the first to quantitatively assess how disease-associated syt1 variants can disrupt neurotransmitter release when expressed alongside WT protein (Fig. 3). Our findings unequivocally demonstrate the capacity for these heterozygous mutations to cause profound impairment of neurotransmitter release (Fig. 3). Moreover, this work provides strong evidence for a graded potency of disease-associated syt1 variants, with D365E exhibiting a markedly less severe dominant-negative phenotype *versus* D303G and I367T (Fig. 3). We note that substantial phenotypic heterogeneity is also observed for each given genotype (Baker et al., 2018), suggesting that allelic expressivity also plays an important role in determining disease severity. It is unknown how WT and mutant alleles vary in expression across brain regions or neuronal subtypes in these patients. However, when controlling for allelic expression ratio, the human D366E variant can be expected to produce a less severe clinical phenotype than either

D304G or I368T—as observed in the limited number of mutation-bearing patients described so far (Baker et al., 2018).

Our biochemical (Fig. 4) and spectroscopic (Fig. 5) studies establish that this graded effect on synaptic physiology (Figs. 2, 3) corresponds well to a graded impact on Ca^{2+} -dependent binding and penetration of membranes by syt1. Across these studies, variants D365E and I367T were more evenly matched, with a trend toward more severe impairment in I367T (Figs. 4, 5). In comparison, variant D303G, which is associated with the most severe human phenotype (Baker et al., 2018) and showed the most substantial impairment of synaptic release at low mutant:WT expression ratios (Fig. 3), also exhibited the most severe biophysical impairments. Our combined results are summarized in Table 2. These data provide strong support for a mechanism of action of syt1 that specifically involves Ca^{2+} -dependent penetration of the plasma membrane to trigger synaptic vesicle fusion (Bai et al., 2016; Evans et al., 2015; Liu et al., 2014). Further studies may define whether these mutations also impact other roles for syt1, such as synaptic vesicle-plasma membrane docking (Chang et al., 2018; Liu et al., 2009).

Functional segregation and positive allostery between the tandem C2 domains of syt1

Our membrane penetration studies (Fig. 5) also reveal several interesting features of a prototypical Ca^{2+} -dependent protein-lipid interaction involving tandem Ca^{2+} -binding domains. To our surprise, the Ca^{2+} responses of C2A and C2B were distinct in WT syt1, with C2B exhibiting a higher-affinity mode of Ca^{2+} -dependent membrane penetration (Fig. 5). While the basis for the higher Ca^{2+} sensitivity of C2B is not clear, this effect is likely due to the substantial cooperativity between Ca^{2+} - and PIP_2 -binding activities of syt1 C2B (Bai et al., 2004; Li et al., 2006; van den Bogaart et al., 2012). Indeed, each disease-associated mutation inhibited Ca^{2+} -dependent membrane penetration (Fig. 5) and dramatically disrupted Ca^{2+} -dependent binding to PIP_2 (Fig. 4). Thus, in addition to binding a polybasic patch on the side of C2B and juxtaposing the cytoplasmic domain of syt1 with the target membrane (Bai et al., 2004), PIP_2 likely interacts with the Ca^{2+} -binding, membrane-inserting residues of C2B. This interpretation is supported by the capacity of PIP_2 to drive Ca^{2+} -independent membrane penetration by syt1 (Bradberry et al., 2019).

An unresolved question regarding the mechanism of action for syt1 concerns the differential sensitivity of its C2-domains to mutations. While mutations in C2A are often well-tolerated (Stevens and Sullivan, 2003), mutations in C2B readily disrupt the function of this protein (Mackler et al., 2002), as evidenced by the clustering of disease-associated mutations in C2B (Baker et al., 2018). The higher Ca^{2+} sensitivity of membrane penetration by C2B (Fig. 5) implies that penetration by this domain liberates more free energy than penetration by C2A and suggests a biochemical basis for the sensitivity of mutations in C2B. This high Ca^{2+} sensitivity may also be critical for the role of C2B in dynamic, Ca^{2+} -dependent docking of synaptic vesicles (Chang et al., 2018). The lower Ca^{2+} sensitivity of C2A (Fig. 5) may serve to enable a wider dynamic range of Ca^{2+} sensitivity for syt1-triggered membrane fusion, which is sensitive to changes in $[\text{Ca}^{2+}]_i$ across a range of $[\text{Ca}^{2+}]_i$ spanning orders of magnitude (Burgalossi et al., 2010; Neher and Sakaba, 2008; Stevens and Sullivan, 2003).

A closely related problem is the question of how and whether C2A and C2B exhibit positive allosterism in terms of Ca^{2+} -dependent membrane binding activity. Several previous studies have suggested a functional link between the two domains that depends on their relative orientations (Bai et al., 2016, 2002; Evans et al., 2016; Herrick et al., 2006; Liu et al., 2014; Tran et al., 2019). However, these studies have not addressed Ca^{2+} cooperativity *per se*, i.e., does Ca^{2+} and lipid binding by one domain drive Ca^{2+} and lipid binding by the other domain? Our penetration studies formally establish a cooperative action between C2A and C2B by demonstrating that mutations in C2B can reduce the Ca^{2+} sensitivity of penetration by C2A (Fig. 5). Our data help establish a clear mechanistic picture for how Ca^{2+} activates syt1: C2B, by binding PIP_2 and penetrating the membrane with high Ca^{2+} sensitivity, drives the adjacent C2A to likewise bind Ca^{2+} and penetrate the membrane to increase release probability (Courtney et al., 2019). The interactions underlying this allosterism are unclear but may involve changes in the membrane-water interface that occur with penetration of the membrane by each C2 domain.

Molecular correlates of synaptic Ca^{2+} cooperativity

Another critical but poorly understood cooperative relationship is the power-law relationship between synaptic vesicle fusion rate and $[\text{Ca}^{2+}]_i$ (Dodge and Rahamimoff, 1967; Neher and Sakaba, 2008). Because syt1 binds 4–5 Ca^{2+} ions (Brose et al., 1992; Fernandez et al., 2001; Shao et al., 1996), this stoichiometry has long been proposed to mediate the Ca^{2+} dependence of synaptic release (Brose et al., 1992). However, in a number of studies, including data reported here, the Ca^{2+} -dependent membrane binding and penetration by syt1 exhibits a far shallower dependence on Ca^{2+} (Brose et al., 1992; Evans et al., 2016; Gaffaney et al., 2008; Tran et al., 2019; van den Bogaart et al., 2012) (Fig. 4, Fig. 5). In particular, the present study demonstrates this relatively low degree of Ca^{2+} cooperativity using two different assays of Ca^{2+} -dependent syt-membrane interaction (Fig. 4, Fig. 5). Our results argue strongly against the notion that the power law relationship between Ca^{2+} and synaptic release is determined by the number of Ca^{2+} binding sites in a single syt1 molecule. The high Ca^{2+} cooperativity of release but low Ca^{2+} cooperativity of membrane penetration by syt1 can be readily reconciled by the participation of multiple copies of syt1 in the membrane fusion reaction. Our finding that disease-associated syt1 variants potentially disrupt the function of WT syt1 at sub-stoichiometric expression ratios, particularly for variant D303G (Fig. 3), supports this notion. Further studies, combining accurate syt1 copy number measurements *in situ* with more rigorous measurements of vesicle release rates, may better define a role for syt1 in the Ca^{2+} cooperativity of neurotransmitter release.

Pharmacologic strategies for treatment of syt1-associated neurodevelopmental disorder

Finally, our mechanistic studies culminated in the discovery that 4-aminopyridine, a drug that is approved for clinical use (Leussink et al., 2018), may help to mitigate the synaptic deficits in syt1-associated neurodevelopmental disorder (Fig. 6). In patients with more severe phenotypes (D304G and I368T, in this series), treatment targets may include reduced agitation and self-injurious behavior. In patients with less severe phenotypes (D366E in this series), targets may include improved attention and learning ability. The concentrations used in this study are higher than, but within fivefold of, typical serum concentrations achieved with standard doses of 4-AP (Bever et al., 1994), and even a partial recovery of presynaptic

function may allow for functional improvement in these patients. We note that neurons and synapses functioning under physiologic conditions may have substantially different responses to 4-AP than those of our hippocampal cultures. We also emphasize that, given the importance of brain developmental processes, any pharmacologic intervention is unlikely to cause complete functional recovery, though this may also depend on the age at which such interventions are initiated. Regardless, given the lack of other viable and specific treatment options, centrally acting K_v blockade by 4-AP appears to be a rational, plausible option for treatment of patients with this profound neurodevelopmental disorder.

STAR METHODS

RESOURCE AVAILABILITY

Lead contact Further information and requests for resources and reagents should be directed to and will be fulfilled by the Lead Contact, Dr. Edwin Chapman (chapman@wisc.edu).
Materials Availability All unique/stable reagents generated in this study are available from the Lead Contact with a completed Materials Transfer Agreement.

Data and Code Availability X-ray crystallography data generated in this study have been deposited at the protein data bank (PDB) with the accession codes 6TZ3 (syt1 C2B WT), 6U41 (syt1 C2B D304G), 6U4W (syt1 C2B D366E), and 6U4U (syt1 C2B I368T). All other source data are available from the corresponding author on request.

EXPERIMENTAL MODEL AND SUBJECT DETAILS

All neuronal cultures were prepared from early postnatal (P0-P1) mouse pups in accordance with all relevant regulations and with the approval of the University of Wisconsin Institutional Animal Care and Use Committee. For some electrophysiologic studies (Fig. 2), pups from *Syt1*^{+/-} breeders (Jackson Labs stock # 002478) were used; for imaging and other electrophysiologic studies (Figs. 2, 3, 6, and S4), pups from *Syt1*^{fl/fl} breeders (Quadros et al., 2017) were used. Mice were maintained on a C57B6/J background. Clinical histories for patients harboring syt1 variants D304G and D366E were obtained through interviews with the parents of these patients and through standard record request protocols. All procedures were performed with the approval of the University of Wisconsin Health Sciences Institutional Review Board.

METHOD DETAILS

Patient genotyping—Sanger sequencing (Functional Biosciences, Madison, WI) was performed following extraction of genomic DNA from saliva samples (Oragene collection kit and Prep-IT L2P reagent, both from DNA Genotek) using the primers: gcaagagaaattgggtgatctgcttctccc (D303G, forward); cgcagcatgtgcgcatgc (D303G, reverse); ggccctatctctagagctagatgattcatattcattcatgc (D365E, forward); cttcttgacggccagcatgcatc (D365E, reverse).

Protein purification and labeling—For crystallography studies, the cDNA encoding human syt1 C2B (amino acids 272–422) was cloned into a pET-based expression vector that included a His6-tagged maltose binding protein and a tobacco etch virus protease (TEV)

restriction site. Site-directed mutagenesis (Stratagene QuikChange) of syt1 C2B was performed to make three single-point mutant constructs. All mutations were confirmed by DNA sequencing. Plasmids containing the recombinant C2B domains were transformed into BL21(DE3) *E. coli*, which were grown in Terrific Broth and induced with IPTG for protein production. The cell pellets were frozen at -80°C and stored until needed. Cells were thawed in lysis buffer [20 mM HEPES (pH 7.4), 150 mM NaCl], lysed using a Microfluidizer, and clarified by centrifugation using a Beckman JA-20 rotor at 19,500 rpm (45,900 g) for 45 min. The supernatant was passed through a Ni-NTA affinity column which was equilibrated with lysis buffer. The column then was washed with 150 ml lysis buffer, followed by a wash in lysis buffer plus 30 mM imidazole. Finally, His₆-MBP-C2B was eluted with 80 ml lysis buffer including 300 mM imidazole. The resulting fusion protein was cleaved with TEV protease overnight at 4°C . Next, an SP-Sepharose column was used to separate the C2B domain from MBP, TEV protease, and uncleaved fusion proteins. Elution from the cation exchange column was done with a 0 to 1 M NaCl gradient and the solution containing the protein of interest was concentrated and loaded onto a Superdex 75 column to remove the remaining contaminants. Purity was assessed using SDS-PAGE Stain-Free gels from BioRad, and protein concentrations were quantified by OD₂₈₀ using each protein's calculated extinction coefficient. For membrane binding and penetration studies, WT and mutant rat syt1 C2AB (residues 96–421), with or without cysteines introduced for labeling, were purified as glutathione-S-transferase fusion constructs (pGEX4T-1 vector, GE healthcare) and eluted by thrombin cleavage as described previously (Bradberry et al., 2019). Labeling was performed using IANBD-amide followed by desalting with size-exclusion chromatography, also as described previously (Bradberry et al., 2019). For SNARE binding assays, HaloTag-syt1 C2AB (pTrcHis vector, Thermo) and the syntaxin1A/SNAP-25B t-SNARE heterodimer (pRSF Duet vector, Novagen) were expressed as N-terminal his₆ fusion constructs, purified by immobilized metal affinity chromatography, and eluted with imidazole as described previously (Bradberry et al., 2019; Courtney et al., 2018).

Crystallization and data collection—The WT syt1 C2B domain was crystallized in 0.2 M ammonium sulfate (pH 6.0), 30% PEG3350 (pH 6.0); the D304G mutant was crystallized in 2.0 M ammonium sulfate (pH: 4.6), 0.1 M sodium acetate; the D366E mutant was crystallized in 1.6 M ammonium sulfate (pH 4.0), 0.1 M citrate; and the I368T mutant was crystallized in 1.5 M ammonium sulfate (pH range: 4.5–4.8), 0.1 M sodium acetate. All crystals were grown at 20°C using the hanging droplet method with purified protein at a stock concentration of 20 mg/ml. The crystals were captured into nylon loops and frozen in liquid N₂. Initial data sets were collected on a Rigaku ScreenMachine. High resolution data sets were collected at SLAC beamline 7–1. The wavelength of each dataset were: wild type 1.097 Å, D304G 0.984 Å, D366E 0.9795 Å, and I368T 1.099 Å and the data were collected at 90 K. X-ray data were processed and scaled using XIA2 (Evans, 2006; Kabsch, 2010; Winn et al., 2011; Winter, 2010; Winter et al., 2018). The X-ray crystal structure was solved using molecular replacement techniques (Phaser) (McCoy et al., 2007) and subsequently refined using Phenix (Adams et al., 2010).

Cell culture and lentiviral transduction.—Briefly, cortices (syt1 WT/KO, data in fig. 2) or hippocampal formations (*Syt1^{fl/fl}*, data in Figs. 3, 6, S4) were obtained by

microdissection and kept in Hibernate-A until the completion of dissection, at which point they were incubated with trypsin-EDTA (Corning, 0.25%) for 30 minutes at 37 °C with periodic agitation. Trypsin was then replaced with plating medium (DMEM +10% FBS) and tissue was triturated 10–20 times with a 1 ml pipette before plating at ~100,000 cells/cm² onto poly-D-lysine coated glass coverslips. Plating medium was replaced with complete growth medium (Neurobasal-A medium supplemented with B-27 (1X, Gibco) and Glutamax (1X, Gibco)) after 1 hour. Lentivirus encoding Cre recombinase under the control of a synapsin promoter and, for imaging experiments, lentivirus encoding a modified iGluSnFR construct were added to cultures at 0–2DIV. Lentivirus encoding WT or mutant syt1 variants was added at 5–7DIV.

Molecular biology and lentiviral preparation for physiology experiments—For lentiviral constructs, DNA sequences encoding WT syt1 or mutant variants generated by site-directed mutagenesis (QuikChange Lightning, Agilent) were subcloned into the FUGW lentiviral transfer plasmid (Addgene plasmid #14883, a gift from Dr. David Baltimore) (Lois, 2002) modified to include the human synapsin promoter and an internal ribosome entry sequence followed by the red fluorescent protein mRuby3. A lentiviral transfer plasmid encoding Cre recombinase under the control of the human synapsin promoter was used in experiments with *Syt1^{fl/fl}* neurons (Addgene plasmid #86641, a gift from Dr. Fan Wang) (Sakurai et al., 2016). Lentivirus was generated by CaPO₄-mediated cotransfection of HEK293-T cells with transfer plasmid and the helper plasmids pCD/NL-BH* (Addgene plasmid #17531, a gift from Dr. Jakob Reiser) (Zhang et al., 2004) and pLTR-G (Addgene plasmid #17532, a gift from Dr. Jakob Reiser) (Reiser et al., 1996) followed by concentration of virus-bearing supernatant by ultracentrifugation as described (Kutner et al., 2009). iGluSnFR (Addgene plasmid # 41732, a gift from Dr. Loren Looger) (Marvin et al., 2013) was modified to remove the final four amino acids and include a Golgi export sequence (Parmar et al., 2014) and ER exit motif (Stockklauser et al., 2001). This construct was subcloned into the FUGW lentiviral transfer plasmid modified to include the CamKII α promoter.

Immunocytochemistry and confocal microscopy—At 14–16 DIV, coverslips of hippocampal neurons from *Syt1^{fl/fl}* mice expressing WT or mutant variant syt1 were rinsed 2–3 times with phosphate-buffered saline (PBS) and fixed by incubation with pre-warmed 4% paraformaldehyde for 10 minutes at 37 °C. Cells were washed in PBS, incubated for 10 minutes in PBS containing 0.2% saponin and 50 mM Tris-HCl pH 8.0, washed in PBS, and blocked for 1 hour at room temperature in PBS containing 5% normal goat serum, 5% BSA, and 0.02% saponin. Coverslips were then incubated with primary antibodies against syt1 (mouse mAb 48, Iowa DSHB (Matthew, 1981), 1:250 dilution of a 3.7 mg/ml stock purified from ascites fluid) and synaptophysin (guinea pig pAb, Synaptic Systems, 1:250 dilution of a 1 mg/ml stock) in PBS containing 1% BSA and 0.02% saponin at 4°C overnight. Coverslips were washed in PBS containing 0.02% saponin and incubated with fluorescent secondary antibodies (AlexaFluor488 conjugated goat anti-guinea pig IgG and AlexaFluor647 conjugated goat anti-mouse IgG2b) for 1 hour at room temperature. Cells were then washed in PBS containing 0.02% saponin, followed by PBS without saponin, and mounted on glass slides. Fixed, stained slides were later imaged on a Zeiss LSM 880

confocal microscope equipped with a 40× 1.3NA oil objective with identical laser power and gain settings used for all experiments. Pearson's correlation coefficients were calculated using the Coloc 2 plugin in FIJI (Schindelin et al., 2012) on z-stack maximum projections without thresholding. Replicates represent single fields of view from at least 2 separate dissections.

Immunoblotting—Coverslips of neurons (14–18 DIV) from *Syt1^{fl/fl}* mice expressing WT or mutant syt1 variants were rinsed 2–3 times in PBS and lysed by repeated pipetting of 150 µl lysis buffer (50 mM Tris pH 8.0, 150 mM NaCl, 2% SDS, 0.1% Triton X-100, 10 mM EDTA) containing protease inhibitors (cOmplete mini EDTA-free, Roche, 1 tablet / 10 ml lysis buffer). These samples were combined with 50 µl 4X Laemmli sample buffer, heated to 70°C for 10 minutes, and stored at –20 °C until use. For each experiment, samples were subjected to SDS-PAGE, transferred to PVDF membrane, blocked in Tris-buffered saline containing 0.1% Tween-20 (TBS-T) with 5% milk, and blotted using an anti-syt1 antibody (mAb 48 (Matthew, 1981), 1:500 dilution of hybridoma supernatant (Developmental Studies Hybridoma Bank)) in TBS-T with 1% milk at 4°C overnight. After washing in TBS-T, blots were incubated with HRP-conjugated goat anti-mouse IgG2b 2° antibody (Invitrogen) in TBS-T for 1 hr at room temperature, washed in TBS-T, and imaged with a CCD gel imaging device (GE). Equal protein loading across lanes was confirmed by Coomassie staining of gels after transfer.

Electrophysiology—Whole-cell voltage-clamp recordings of cultured neurons (13–16DIV) were performed at room temperature in a bath containing (in mM): 128 NaCl, 5 KCl, 1 MgCl₂, 2 CaCl₂ 25 HEPES-NaOH, 30 glucose) using patch pipettes pulled from borosilicate glass (Sutter instruments, 1.5 mm OD, 1.1 mm ID, 3–5 MOhm) with an internal solution containing (in mM): 130 KCl, 1 EGTA, 10 HEPES-NaOH, 2 ATP (Mg salt), 0.3 GTP (Na salt), 5 phosphocreatine (Na salt). Recordings were performed using a MultiClamp 700B combined amplifier and digitizer (Molecular Devices) under the control of Clampex 10 software (Molecular Devices) (Fig 2) or using a HEKA EPC 10 combined amplifier and digitizer under the control of HEKA PatchMaster software (Fig. S4). GABA_A-mediated currents were isolated using CNQX (20 µM) and APV (50 µM); for mIPSC recordings, 1 µM TTX was included in the bath. QX-314 chloride (5 mM) was included in the pipette solution for evoked synaptic recordings. Neurons were held at –70 mV in all experiments without correction for liquid junction potentials. Series resistance was monitored, and recordings were discarded if this quantity rose above 15 MOhms. For evoked recordings, a concentric bipolar electrode (FHC, 125/50 um extended tip) was placed 100–200 um away from the patched soma and stimulation currents were adjusted evoke maximal responses. For mIPSC recordings, sixty seconds of data were recorded for each cell. mIPSCs were quantified for each recording using a template-matching algorithm in Clampfit (Molecular Devices). Each replicate represents an individual cell from at least 2 separate dissections.

Glutamate imaging—All experiments were performed at room temperature. Imaging bath solution contained (in mM): 128 NaCl, 2.5 KCl, 1 MgCl₂, 2 CaCl₂, 25 HEPES-NaOH, 30 glucose; complete blockade of synaptic currents was achieved using CNQX (20 µM), APV (50 µM), and picrotoxin (50 µM). Coverslips were mounted in a field stimulus chamber

(RC-49MFSH, Warner Instruments) and imaged on a motorized inverted epifluorescence microscope (Olympus IX81) equipped with a 60x, 1.45 NA oil immersion objective (Olympus) and standard GFP filter set (49002, Chroma). Illumination was provided with a 470 nm LED (Thorlabs) and fluorescence was detected on the central quadrant of an sCMOS camera (OrcaFLASH V2.0, Hamamatsu) operated in 4×4 binning mode (256 × 256 pixels, 111 × 111 μm field of view) using a 10 ms exposure time. The optical setup was controlled using Micro-Manager (Edelstein et al., 2010), with LED intensity controlled using a USB DAQ (National Instruments). Stimulus control was accomplished using the DAQ of a HEKA EPC 10 combined amplifier and digitizer connected to the timing input of the sCMOS camera and controlled with PatchMaster software. Stimuli (100 V, 0.5 ms) were delivered using a stimulation box (Grass SX88). For each coverslip, responses to 10-AP, 10-Hz stimulus trains were acquired with at least 4 minutes of rest in between acquisitions. dF/F_0 was calculated for the whole field of view to normalize for the amount of sensor present, with baseline subtraction determined using a dark area of the coverslip. For experiments involving 4-AP treatment, the microscope was equipped with a motorized XY stage (Mad City Labs) and the same fields of view were imaged in control and 4-AP conditions. Conversion of raw fluorescence to dF/F_0 was performed using a custom-written R script. Replicates were defined as average traces for a whole coverslip (Fig. 3) or fields of view (Fig. 6) across 2–5 separate dissections.

Liposome preparation—Liposomes were prepared by evaporation from chloroform:methanol lipid stocks (all from Avanti Polar lipids), rehydration at 10 mM [lipid] in reconstitution buffer (25 mM HEPES-NaOH pH 7.4, 100 mM KCl), and extrusion as described (Bradberry et al., 2019). In Fig. 4B-C, liposomes contained 30% POPE and the indicated amount of POPS and PIP₂, with the remainder comprising POPC. For Fig. 4D-H, liposomes contained 35% cholesterol, 25% POPC, 15% POPS, 20% POPE, 5% phosphatidylinositol, and 1% PIP₂; for Fig. 5, liposomes contained 35% cholesterol, 23% POPC, 15% POPS, 20% POPE, 5% phosphatidylinositol, and 3% PIP₂.

Cosedimentation assays—In Fig. 4B-C, liposomes (2 mM [lipid]) were mixed with C2AB (4 μM) in reconstitution buffer containing 0.5 mM EGTA in volume of 100 μl; where indicated, 1.5 mM Ca²⁺ was added, yielding 1.0 mM [Ca]_{free}. Reaction mixtures were incubated with shaking for 30 minutes, transferred to small polycarbonate centrifuge tubes, and centrifuged at 65,000 RPM in a TLA-100 rotor (Beckman). Supernatants were combined with Laemmli sample buffer, subjected to SDS-PAGE, and C2AB was detected by staining with Coomassie Brilliant Blue. For Fig. 4D-E, conditions were the same except that the reconstitution buffer contained 5 mM nitrilotriacetic acid (NTA) and 1 mM EGTA (pH 7.4), along with 0–5 mM CaCl₂. [Ca²⁺]_{free} in these buffers was established using home-built Ca²⁺ minielectrodes (Bers et al., 2010; Hove-Madsen et al., 2010). For fig. S7, NBD-C2AB (250 nM) was combined with liposomes of the same formulation in reconstitution buffer containing 5 mM NTA and 1 mM EGTA. This mixture was immediately centrifuged at 90,000 RPM in a TLA-100 rotor, the supernatants mixed with Laemmli buffer and subjected to SDS-PAGE, and the labeled C2AB was detected by in-gel fluorescence with a CCD gel imaging device (GE). Independent experiments were defined as replicates performed with separately prepared batches of C2AB and liposomes.

Syt1-t-SNARE binding assays—Binding assays were performed as described previously (Courtney et al., 2018). Briefly, purified WT or mutant C2AB protein containing an N-terminal HaloTag was bound to HaloLink beads, the beads were washed, and these Halo-C2AB beads were incubated with purified t-SNARE heterodimer in buffer containing 150 mM NaCl, 25 mM HEPES-NaOH pH 7.4, 1% Triton X-100, and 1 mM EGTA +/- 1.5 mM CaCl₂ for 30 minutes at room temperature with rotation. The beads were washed (3 × 1 ml) in the same buffer and the bound t-SNAREs eluted with Laemmli sample buffer. This eluate was subjected to SDS-PAGE and t-SNAREs were detected by Coomassie staining. Independent experiments were defined as replicates performed with separately prepared batches of C2AB and t-SNAREs.

Stopped-flow rapid mixing—Syt1 C2AB (4 μM), liposomes (1 mM), and CaCl₂ (250 μM) were combined in reconstitution buffer and loaded into one syringe of an SX-18.MV stopped-flow spectrometer (Applied Photophysics). The second syringe of the stopped-flow device was filled with quin-2 (500 μM) in reconstitution buffer. Equal volumes from the two syringes were rapidly mixed at room temperature while monitoring quin-2 fluorescence. Excitation at 335 nm was provided by a xenon arc lamp via monochromator while emission was monitored via a 470 nm long-pass filter (KV470, Schott). Exponential decays were fitted using Prism (GraphPad) before normalization, with the first 1.5 ms of each trace omitted to account for instrument dead time. Independent experiments were defined as replicates performed with a unique combination of separately prepared batches of protein and lipid.

Penetration assays—Labeled syt1 C2AB (250 nM) and liposomes (0.6 mM) were combined in reconstitution buffer containing 5 mM NTA, 1 mM EGTA, pH 7.4 (500 μl total volume) in a quartz cuvette. CaCl₂ (100 mM or 1 M reference solutions) were added to achieve the [Ca²⁺]_{free} indicated in Fig. 5. Spectra (470 nm excitation, 490–630 nm emission scan) were acquired before and after the addition of lipids, as well as after each Ca²⁺ addition, using a fluorimeter with excitation and emission monochromator slits set to 4 nm (Photon Technology International). Spectra were corrected for scattering using a lipid blank, and additional scattering after addition of Ca²⁺ did not contribute substantially to the observed signal in the [Ca²⁺]_{free} range used. dF/F₀ values were calculated by averaging the raw, baseline-corrected intensity from 510–610 nm and normalizing to the fluorescence observed prior to the addition of Ca²⁺. Independent experiments were defined as replicates performed with separately prepared batches of protein and lipid.

QUANTIFICATION AND STATISTICAL ANALYSIS

All electrophysiological data in Fig. 2 were acquired and analyzed by an investigator blinded to the genotype of each condition. All other data were collected and analyzed in a non-blinded fashion. Values are reported as mean ± standard error of the mean (SEM), mean ± standard error (SE) of the fit parameter, or mean with 95% confidence interval as indicated in the figure legends. Replicates are defined as indicated in the corresponding Methods sections and in the figure legends. All data were tested for normality prior to choosing the appropriate statistical test. No estimation of required sample sizes was performed. All statistical analysis was performed using Prism (GraphPad).

ADDITIONAL RESOURCES

Detailed clinical histories for patients D304G and D366E—The first proband, a now 26-year-old male with a D304G variant in *SYT1*, was born to a 26-year-old G1P1 mother, the product of a 42.5 week gestation uncomplicated pregnancy. Parents were nonconsanguineous; family history was significant for paternal relatives with porphyria (although his father’s genetic testing was negative), dyslexia in his mother and intellectual disability in a paternal first cousin. He was born via uncomplicated c-section following induction with failure to progress. An elevated white counted prompted a sepsis rule-out which was unremarkable. Developmental delay was first evaluated at four months of age, when he did not regard objects or have purposeful movements. He rolled over at five months, had some head control at eight months, reached at nine months, and grabbed objects at 12 months. At 15 months, he was unable to sit up but could maintain sitting posture. He pulled to sit and scooted in a seated position at three years, crawled at five years, and pulled to stand at six years. He reportedly smiled and laughed sometime before four months, recognized parents at four months, cooed at five months, and babbled at 2.5 years. He never went on to use words. Self-stimulatory behaviors emerged at four years of age, which evolved into episodes of self-injurious behavior (repeatedly beating chest and face or banging his head on the floor). These were treated with clonidine 0.2mg at bedtime and fluoxetine 40mg daily. Episodes of agitation and self-injurious behavior later required the addition of lamotrigine, risperidone, and valproic acid. Due to trouble maintaining weight and poor feeding attributed to severe gastroesophageal reflux, a g-tube was placed at 15 years old. He had a spinal fusion with rod placement for scoliosis at 16 years old, after which he did not recover the ability to crawl or sit independently.

At 16 months, he was 25% for weight, 75% for height, and 25–50% for head circumference; at 23 months head circumference was stable at 50%, but weight and height had dropped to less than 5%. He was hypotonic on initial neurologic exam; he subsequently was noted to have a right Babinski sign at 2.5 years, and a bilateral Babinski signs at four years. He had a normal retinal exam at four years of age. Eventually he developed spasticity, which was treated with baclofen 10mg BID. Initial workup performed at six months was normal and included MRI (reportedly normal other than borderline immature myelination), EEG (reportedly normal), karyotype, Fragile X DNA analysis, blood and urine amino acids, urine organic acids, serum carnitine, and TSH. Hearing test including auditory brainstem responses was normal. MRI brain was repeated at 18 months and showed immature myelination in bilateral frontal and temporal lobes. MRI at four years was normal. EEG awake and asleep at four years old showed no PDR, frequent multifocal spikes (T6, T5, F3, P4) and rare generalized spikes, although it did show normal sleep spindles. Tests for GM1 and GM2 gangliosidosis, phytanic acids, CLCFA, plasma and urine carnitine, MPS and CPK were all normal. Urine oligosaccharides did not show consistent abnormalities. Testing for NCL disorders and Angelman (FISH and subsequent methylation studies) were normal. Whole exome sequencing (GeneDx XomeDxPlus, mean depth of coverage 165x, quality threshold 97.3%) at 21 years old showed normal mitochondrial DNA, variants of unknown significance in *CCDC22* (his mother was heterozygous for this variant; it had not been previously reported, other substations at this location have been well tolerated, and in-silico analysis predicted it to be benign), *FOXP1* (his father was heterozygous for this variant; it

had not previously been identified in population databases, is not conserved across species, is a conservative substitution unlikely to affect function, and in silico analysis was inconclusive), and KIF5C (his mother was heterozygous for this variant, it had not been previously described in population databases, is conserved across species, may impact secondary protein structure, and in-silico analysis was inconclusive). These were not thought to contribute to the patient's disorder. Additionally, a *de novo* variant in SYT1 (p.D304G) was identified, which was examined in the present study.

The second proband, a now six-year-old female with a D366E variant in SYT1, was born to a G2P2 mother, the product of a 39-week gestation pregnancy with no complications. Parents were non-consanguineous; family history was significant only for a maternal cousin with Noonan syndrome. She was born via spontaneous vaginal delivery with no complications. Snoring was noted at one month, and a sleep study at three months showed severe obstructive sleep apnea with central apneas (apnea hypopnea index 36.7, obstructive apnea (OSA) index 27.8). An atrial septal defect noted at two months on echocardiogram closed spontaneously. She had poor weight gain, and a swallow study at three months old showed disorganized swallowing. Supraglottoplasty at four months of age improved swallowing function with subsequent weight gain, and sleep study at seven months showed moderate but improved OSA. She was evaluated by ophthalmology at five months of age, who noted esotropia and delayed visual maturation. She underwent corrective surgery at ten months of age with resolution of esotropia, and ophthalmology exam at 20 months was normal.

Developmental delay was noted at seven months. She achieved unsteady sitting at ten months, crawling and sitting without support at 15 months, pulled to stand at 20 months, and walked at 28 months. She developed pincer grasp at 20 months. She smiled at ten months, babbled at 13 months, and spoke two words at two years old. At four years old, she could run, feed herself, use a pincer grasp, and had four words (yeah, dah, down, up). She has no history of developmental regression.

At 13 and 45 months, head circumference and height were 50%, whereas weight was 5%. She had no dysmorphic features, and neuro exam was significant only for hypotonia. Karyotype and high resolution chromosomes, methylation tests for Angelman, Rett MECP2 del/dup, Joubert sequencing panel, serum amino acids, urine organic acids, acyl-carnitine panel, disorders of glycosylation, urinary creatine and guanidinoacetate, urinary purine panel, urine pyrimidine panel, serum creatine/GAA, very long chain fatty acids, CK were all normal. Visual evoked potentials at 6 months showed reduced amplitude PVEP (right eye amplitude 50% of left) with prolonged latency of 120ms bilaterally. Routine EEG at 2.5 years was abnormal due to occipital intermittent rhythmic delta activity and background slowing, primarily comprised of 30–40 μ V 3–4Hz delta activity. Mitochondrial genome sequencing was normal. Whole exome sequencing (Gene Dx XomeDxPlus, mean depth of coverage 84x, quality threshold 95.4%) identified a *de novo* variant in SYT1 (p.D366E), which was examined in the present study.

Supplementary Material

Refer to Web version on PubMed Central for supplementary material.

ACKNOWLEDGMENTS

We thank Dr. Jason Vevea for designing the improved iGluSnFR construct and members of the Chapman Lab for providing helpful discussion. This work was funded by the Howard Hughes Medical Institute (Investigator Grant to E.R.C.) and the National Institutes of Health (grant MH116580 to M.M.B.; grants MH061876 and NS097362 to E.R.C.; grant AR063634 to R.B.S.). E.R.C. is an Investigator of the Howard Hughes Medical Institute.

REFERENCES

- Adams PD, Afonine PV, Bunkóczi G, Chen VB, Davis IW, Echols N, Headd JJ, Hung L-W, Kapral GJ, Grosse-Kunstleve RW, McCoy AJ, Moriarty NW, Oeffner R, Read RJ, Richardson DC, Richardson JS, Terwilliger TC, Zwart PH, 2010 *PHENIX*: a comprehensive Python-based system for macromolecular structure solution. *Acta Crystallogr. D Biol. Crystallogr.* 66, 213–221. 10.1107/S0907444909052925 [PubMed: 20124702]
- Alle H, Kubota H, Geiger JRP, 2011 Sparse But Highly Efficient Kv3 Outpace BKCa Channels in Action Potential Repolarization at Hippocampal Mossy Fiber Boutons. *J. Neurosci.* 31, 8001–8012. 10.1523/JNEUROSCI.0972-11.2011 [PubMed: 21632922]
- Bai H, Xue R, Bao H, Zhang L, Yethiraj A, Cui Q, Chapman ER, 2016 Different states of synaptotagmin regulate evoked versus spontaneous release. *Nat. Commun.* 7, 10971 10.1038/ncomms10971 [PubMed: 27001899]
- Bai J, Tucker WC, Chapman ER, 2004 PIP2 increases the speed of response of synaptotagmin and steers its membrane-penetration activity toward the plasma membrane. *Nat. Struct. Mol. Biol.* 11, 36–44. 10.1038/nsmb709 [PubMed: 14718921]
- Bai J, Wang P, Chapman ER, 2002 C2A activates a cryptic Ca²⁺-triggered membrane penetration activity within the C2B domain of synaptotagmin I. *Proc. Natl. Acad. Sci.* 99, 1665–1670. 10.1073/pnas.032541099 [PubMed: 11805296]
- Baker K, Gordon SL, Grozeva D, van Kogelenberg M, Roberts NY, Pike M, Blair E, Hurles ME, Chong WK, Baldeweg T, Kurian MA, Boyd SG, Cousin MA, Raymond FL, 2015 Identification of a human synaptotagmin-1 mutation that perturbs synaptic vesicle cycling. *J. Clin. Invest.* JCI79765. 10.1172/JCI79765
- Baker K, Gordon SL, Melland H, Bumbak F, Scott DJ, Jiang TJ, Owen D, Turner BJ, Boyd SG, Rossi M, Al-Raqad M, Elpeleg O, Peck D, Mancini GMS, Wilke M, Zollino M, Marangi G, Weigand H, Borggraefe I, Haack T, Stark Z, Sadedin S, Broad Center for Mendelian Genomics, Tan TY, Jiang Y, Gibbs RA, Ellingwood S, Amaral M, Kelley W, Kurian MA, Cousin MA, Raymond FL, 2018 SYT1-associated neurodevelopmental disorder: a case series. *Brain.* 10.1093/brain/awy209
- Bers DM, Patton CW, Nuccitelli R, 2010 A Practical Guide to the Preparation of Ca²⁺ Buffers, in: *Methods in Cell Biology.* Elsevier, pp. 1–26. 10.1016/B978-0-12-374841-6.00001-3
- Bever CT, Young D, Anderson PA, Krumholz A, Conway K, Leslie J, Eddington N, Plaisance KI, Panitch HS, Dhib-Jalbut S, Fessler MJ, Devane J, Johnson KP, 1994 The effects of 4-aminopyridine in multiple sclerosis patients: Results of a randomized, placebo-controlled, double-blind, concentration-controlled, crossover trial. *Neurology* 44, 1054–1054. 10.1212/WNL.44.6.1054 [PubMed: 8208399]
- Bhalla A, Chicka MC, Tucker WC, Chapman ER, 2006 Ca²⁺-synaptotagmin directly regulates t-SNARE function during reconstituted membrane fusion. *Nat. Struct. Mol. Biol.* 13, 323–330. 10.1038/nsmb1076 [PubMed: 16565726]
- Bhalla A, Tucker WC, Chapman ER, 2005 Synaptotagmin Isoforms Couple Distinct Ranges of Ca²⁺-, Ba²⁺-, and Sr²⁺-Concentration to SNARE-mediated Membrane Fusion-D. *Mol. Biol. Cell* 16, 10.
- Bradberry MM, Bao H, Lou X, Chapman ER, 2019 Phosphatidylinositol 4,5-bisphosphate drives Ca²⁺-independent membrane penetration by the tandem C2 domain proteins synaptotagmin-1 and Doc2β. *J. Biol. Chem.* 294, 10942–10953. 10.1074/jbc.RA119.007929 [PubMed: 31147445]

- Brose N, Brunger A, Cafiso D, Chapman ER, Diao J, Hughson FM, Jackson MB, Jahn R, Lindau M, Ma C, Rizo J, Shin Y-K, Söllner TH, Tamm L, Yoon T-Y, Zhang Y, 2019 Synaptic vesicle fusion: today and beyond. *Nat. Struct. Mol. Biol.* 26, 663–668. 10.1038/s41594-019-0277-z [PubMed: 31384060]
- Brose N, Petrenko AG, Südhof TC, Jahn R, 1992 Synaptotagmin: A Calcium Sensor on the Synaptic Vesicle Surface. *Sci. New Ser.* 256, 1021–1025.
- Burgalossi A, Jung S, Meyer G, Jockusch WJ, Jahn O, Taschenberger H, O'Connor VM, Nishiki T, Takahashi M, Brose N, Rhee J-S, 2010 SNARE Protein Recycling by α SNAP and β SNAP Supports Synaptic Vesicle Priming. *Neuron* 68, 473–487. 10.1016/j.neuron.2010.09.019 [PubMed: 21040848]
- Chang S, Trimbuch T, Rosenmund C, 2018 Synaptotagmin-1 drives synchronous Ca^{2+} -triggered fusion by C2B-domain-mediated synaptic-vesicle-membrane attachment. *Nat. Neurosci.* 21, 33–40. 10.1038/s41593-017-0037-5 [PubMed: 29230057]
- Chapman ER, 2008 How Does Synaptotagmin Trigger Neurotransmitter Release? *Annu. Rev. Biochem.* 77, 615–641. 10.1146/annurev.biochem.77.062005.101135 [PubMed: 18275379]
- Courtney NA, Bao H, Briguglio JS, Chapman ER, 2019 Synaptotagmin I clamps synaptic vesicle fusion in mammalian neurons independent of complexin. *Nat. Commun.* 10, 4076 10.1038/s41467-019-12015-w [PubMed: 31501440]
- Courtney NA, Briguglio JS, Bradberry MM, Greer C, Chapman ER, 2018 Excitatory and Inhibitory Neurons Utilize Different Ca^{2+} Sensors and Sources to Regulate Spontaneous Release. *Neuron* 98, 977–991.e5. 10.1016/j.neuron.2018.04.022 [PubMed: 29754754]
- Dodge FA, Rahamimoff R, 1967 Co-operative action of calcium ions in transmitter release at the neuromuscular junction. *J. Physiol.* 193, 419–432. 10.1113/jphysiol.1967.sp008367 [PubMed: 6065887]
- Eberhard DA, Cooper CL, Low MG, Holz RW, 1990 Evidence that the inositol phospholipids are necessary for exocytosis. Loss of inositol phospholipids and inhibition of secretion in permeabilized cells caused by a bacterial phospholipase C and removal of ATP. *Biochem. J.* 268, 15–25. 10.1042/bj2680015 [PubMed: 2160809]
- Edelstein A, Amodaj N, Hoover K, Vale R, Stuurman N, 2010 Computer Control of Microscopes Using μ Manager, in: Ausubel FM, Brent R, Kingston RE, Moore DD, Seidman JG, Smith JA, Struhl K (Eds.), *Current Protocols in Molecular Biology*. John Wiley & Sons, Inc., Hoboken, NJ, USA, p. mb1420s92. 10.1002/0471142727.mb1420s92
- Evans CS, He Z, Bai H, Lou X, Jeggle P, Sutton RB, Edwardson JM, Chapman ER, 2016 Functional analysis of the interface between the tandem C2 domains of synaptotagmin-I. *Mol. Biol. Cell* 27, 979–989. 10.1091/mbc.E15-07-0503 [PubMed: 26792839]
- Evans CS, Ruhl DA, Chapman ER, 2015 An Engineered Metal Sensor Tunes the Kinetics of Synaptic Transmission. *J. Neurosci.* 35, 11769–11779. 10.1523/JNEUROSCI.1694-15.2015 [PubMed: 26311762]
- Evans P, 2006 Scaling and assessment of data quality. *Acta Crystallogr. D Biol. Crystallogr.* 62, 72–82. 10.1107/S0907444905036693 [PubMed: 16369096]
- Fernandez I, Araç D, Ubach J, Gerber SH, Shin O-H, Gao Y, Anderson RG, Südhof TC, Rizo J, 2001 Three-dimensional structure of the synaptotagmin I C2B-domain: synaptotagmin I as a phospholipid binding machine. *Neuron* 32, 1057–1069. [PubMed: 11754837]
- Gaffaney JD, Dunning FM, Wang Z, Hui E, Chapman ER, 2008 Synaptotagmin C2B Domain Regulates Ca^{2+} -triggered Fusion *in Vitro*: CRITICAL RESIDUES REVEALED BY SCANNING ALANINE MUTAGENESIS. *J. Biol. Chem.* 283, 31763–31775. 10.1074/jbc.M803355200 [PubMed: 18784080]
- Herrick DZ, Sterbling S, Rasch KA, Hinderliter A, Cafiso DS, 2006 Position of Synaptotagmin I at the Membrane Interface: Cooperative Interactions of Tandem C2 Domains †. *Biochemistry* 45, 9668–9674. 10.1021/bi060874j [PubMed: 16893168]
- Hove-Madsen L, Baudet S, Bers DM, 2010 Making and Using Calcium-Selective Mini- and Microelectrodes, in: *Methods in Cell Biology*. Elsevier, pp. 67–89. 10.1016/B978-0-12-374841-6.00003-7

- Hui E, Johnson CP, Yao J, Dunning FM, Chapman ER, 2009 Synaptotagmin-Mediated Bending of the Target Membrane Is a Critical Step in Ca²⁺-Regulated Fusion. *Cell* 138, 709–721. 10.1016/j.cell.2009.05.049 [PubMed: 19703397]
- Kabsch W, 2010 XDS. *Acta Crystallogr. D Biol. Crystallogr.* 66, 125–132. 10.1107/S0907444909047337 [PubMed: 20124692]
- Katz B, Miledi R, 1967 The timing of calcium action during neuromuscular transmission. *J. Physiol.* 189, 535–544. 10.1113/jphysiol.1967.sp008183 [PubMed: 6040160]
- Kiessling V, Kreutzberger AJB, Liang B, Nyenhuis SB, Seelheim P, Castle JD, Cafiso DS, Tamm LK, 2018 A molecular mechanism for calcium-mediated synaptotagmin-triggered exocytosis. *Nat. Struct. Mol. Biol.* 25, 911–917. 10.1038/s41594-018-0130-9 [PubMed: 30291360]
- Kutner RH, Zhang X-Y, Reiser J, 2009 Production, concentration and titration of pseudotyped HIV-1-based lentiviral vectors. *Nat. Protoc.* 4, 495–505. 10.1038/nprot.2009.22 [PubMed: 19300443]
- Lee J, Guan Z, Akbergenova Y, Littleton JT, 2013 Genetic Analysis of Synaptotagmin C2 Domain Specificity in Regulating Spontaneous and Evoked Neurotransmitter Release. *J. Neurosci.* 33, 187–200. 10.1523/JNEUROSCI.3214-12.2013 [PubMed: 23283333]
- Leussink VI, Montalban X, Hartung H-P, 2018 Restoring Axonal Function with 4-Aminopyridine: Clinical Efficacy in Multiple Sclerosis and Beyond. *CNS Drugs* 32, 637–651. 10.1007/s40263-018-0536-2 [PubMed: 29992409]
- Li L, Shin O-H, Rhee J-S, Araç D, Rah J-C, Rizo J, Südhof T, Rosenmund C, 2006 Phosphatidylinositol Phosphates as Co-activators of Ca²⁺ Binding to C₂ Domains of Synaptotagmin I. *J. Biol. Chem.* 281, 15845–15852. 10.1074/jbc.M600888200 [PubMed: 16595652]
- Liu H, Bai H, Xue R, Takahashi H, Edwardson JM, Chapman ER, 2014 Linker mutations reveal the complexity of synaptotagmin 1 action during synaptic transmission. *Nat. Neurosci.* 17, 670–677. 10.1038/nn.3681 [PubMed: 24657966]
- Liu H, Dean C, Arthur CP, Dong M, Chapman ER, 2009 Autapses and Networks of Hippocampal Neurons Exhibit Distinct Synaptic Transmission Phenotypes in the Absence of Synaptotagmin I. *J. Neurosci.* 29, 7395–7403. 10.1523/JNEUROSCI.1341-09.2009 [PubMed: 19515907]
- Lois C, 2002 Germline Transmission and Tissue-Specific Expression of Transgenes Delivered by Lentiviral Vectors. *Science* 295, 868–872. 10.1126/science.1067081 [PubMed: 11786607]
- Mackler JM, Drummond JA, Loewen CA, Robinson IM, Reist NE, 2002 The C2B Ca²⁺-binding motif of synaptotagmin is required for synaptic transmission in vivo. *Nature* 418, 340–344. 10.1038/nature00846 [PubMed: 12110842]
- Marvin JS, Borghuis BG, Tian L, Cichon J, Harnett MT, Akerboom J, Gordus A, Renninger SL, Chen T-W, Bargmann CI, Orger MB, Schreiter ER, Demb JB, Gan W-B, Hires SA, Looger LL, 2013 An optimized fluorescent probe for visualizing glutamate neurotransmission. *Nat. Methods* 10, 162–170. 10.1038/nmeth.2333 [PubMed: 23314171]
- Matthew WD, 1981 Identification of a synaptic vesicle-specific membrane protein with a wide distribution in neuronal and neurosecretory tissue. *J. Cell Biol.* 91, 257–269. 10.1083/jcb.91.1.257 [PubMed: 7298720]
- McCoy AJ, Grosse-Kunstleve RW, Adams PD, Winn MD, Storoni LC, Read RJ, 2007 *Phaser* crystallographic software. *J. Appl. Crystallogr.* 40, 658–674. 10.1107/S0021889807021206 [PubMed: 19461840]
- Micheva KD, Holz RW, Smith SJ, 2001 Regulation of presynaptic phosphatidylinositol 4,5-bisphosphate by neuronal activity. *J. Cell Biol.* 154, 355–368. 10.1083/jcb.200102098 [PubMed: 11470824]
- Nalefski EA, Wisner MA, Chen JZ, Sprang SR, Fukuda M, Mikoshiba K, Falke JJ, 2001 C2 Domains from Different Ca²⁺ Signaling Pathways Display Functional and Mechanistic Diversity †. *Biochemistry* 40, 3089–3100. 10.1021/bi001968a [PubMed: 11258923]
- Neher E, Sakaba T, 2008 Multiple Roles of Calcium Ions in the Regulation of Neurotransmitter Release. *Neuron* 59, 861–872. 10.1016/j.neuron.2008.08.019 [PubMed: 18817727]
- Nishiki T. -i., Augustine GJ, 2004 Dual Roles of the C2B Domain of Synaptotagmin I in Synchronizing Ca²⁺-Dependent Neurotransmitter Release. *J. Neurosci.* 24, 8542–8550. 10.1523/JNEUROSCI.2545-04.2004 [PubMed: 15456828]

- Park Y, Seo JB, Fraind A, Pérez-Lara A, Yavuz H, Han K, Jung S-R, Kattan I, Walla PJ, Choi M, Cafiso DS, Koh D-S, Jahn R, 2015 Synaptotagmin-1 binds to PIP2-containing membrane but not to SNAREs at physiological ionic strength. *Nat. Struct. Mol. Biol.* 22, 815–823. 10.1038/nsmb.3097 [PubMed: 26389740]
- Parmar HB, Barry C, Kai F, Duncan R, 2014 Golgi complex–plasma membrane trafficking directed by an autonomous, tribasic Golgi export signal. *Mol. Biol. Cell* 25, 866–878. 10.1091/mbc.e13-07-0364 [PubMed: 24451258]
- Quadros RM, Miura H, Harms DW, Akatsuka H, Sato T, Aida T, Redder R, Richardson GP, Inagaki Y, Sakai D, Buckley SM, Seshacharyulu P, Batra SK, Behlke MA, Zeiner SA, Jacobi AM, Izu Y, Thoreson WB, Urness LD, Mansour SL, Ohtsuka M, Gurumurthy CB, 2017 Easi-CRISPR: a robust method for one-step generation of mice carrying conditional and insertion alleles using long ssDNA donors and CRISPR ribonucleoproteins. *Genome Biol.* 18, 92. 10.1186/s13059-017-1220-4 [PubMed: 28511701]
- Reiser J, Harmison G, Kluepfel-Stahl S, Brady RO, Karlsson S, Schubert M, 1996 Transduction of nondividing cells using pseudotyped defective high-titer HIV type 1 particles. *Proc. Natl. Acad. Sci.* 93, 15266–15271. 10.1073/pnas.93.26.15266 [PubMed: 8986799]
- Reist NE, Buchanan J, Li J, DiAntonio A, Buxton EM, Schwarz TL, 1998 Morphologically Docked Synaptic Vesicles Are Reduced in *synaptotagmin* Mutants of *Drosophila*. *J. Neurosci.* 18, 7662–7673. 10.1523/JNEUROSCI.18-19-07662.1998 [PubMed: 9742137]
- Sakurai K, Zhao S, Takatoh J, Rodriguez E, Lu J, Leavitt AD, Fu M, Han B-X, Wang F, 2016 Capturing and Manipulating Activated Neuronal Ensembles with CANE Delineates a Hypothalamic Social-Fear Circuit. *Neuron* 92, 739–753. 10.1016/j.neuron.2016.10.015 [PubMed: 27974160]
- Schindelin J, Arganda-Carreras I, Frise E, Kaynig V, Longair M, Pietzsch T, Preibisch S, Rueden C, Saalfeld S, Schmid B, Tinevez J-Y, White DJ, Hartenstein V, Eliceiri K, Tomancak P, Cardona A, 2012 Fiji: an open-source platform for biological-image analysis. *Nat. Methods* 9, 676–682. 10.1038/nmeth.2019 [PubMed: 22743772]
- Shao X, Davletov BA, Sutton RB, Sdhof TC, Rizo J, 1996 Bipartite Ca²⁺-Binding Motif in C2 Domains of Synaptotagmin and Protein Kinase C. *Science* 273, 248–251. 10.1126/science.273.5272.248 [PubMed: 8662510]
- Shao X, Fernandez I, Südhof TC, Rizo J, 1998 Solution Structures of the Ca²⁺-free and Ca²⁺-bound C₂A Domain of Synaptotagmin I: Does Ca²⁺ Induce a Conformational Change? †. *Biochemistry* 37, 16106–16115. 10.1021/bi981789h [PubMed: 9819203]
- Shin O-H, Xu J, Rizo J, Südhof TC, 2009 Differential but convergent functions of Ca²⁺ binding to synaptotagmin-1 C2 domains mediate neurotransmitter release. *Proc. Natl. Acad. Sci.* 106, 16469–16474. 10.1073/pnas.0908798106 [PubMed: 19805322]
- Stevens CF, Sullivan JM, 2003 The Synaptotagmin C2A Domain Is Part of the Calcium Sensor Controlling Fast Synaptic Transmission. *Neuron* 39, 299–308. 10.1016/S0896-6273(03)00432-X [PubMed: 12873386]
- Stockklausner C, Ludwig J, Ruppertsberg JP, Klöcker N, 2001 A sequence motif responsible for ER export and surface expression of Kir2.0 inward rectifier K⁺ channels. *FEBS Lett.* 493, 129–133. 10.1016/S0014-5793(01)02286-4 [PubMed: 11287009]
- Südhof TC, Rothman JE, 2009 Membrane Fusion: Grappling with SNARE and SM Proteins. *Science* 323, 474–477. 10.1126/science.1161748 [PubMed: 19164740]
- Sutton RB, Davletov BA, Berghuis AM, Südhof TC, Sprang SR, 1995 Structure of the first C2 domain of synaptotagmin I: A novel Ca²⁺/phospholipid-binding fold. *Cell* 80, 929–938. 10.1016/0092-8674(95)90296-1 [PubMed: 7697723]
- Tran HT, Anderson LH, Knight JD, 2019 Membrane-Binding Cooperativity and Coinsertion by C2AB Tandem Domains of Synaptotagmins 1 and 7. *Biophys. J.* 116, 1025–1036. 10.1016/j.bpj.2019.01.035 [PubMed: 30795874]
- Tucker WC, 2004 Reconstitution of Ca²⁺-Regulated Membrane Fusion by Synaptotagmin and SNAREs. *Science* 304, 435–438. 10.1126/science.1097196 [PubMed: 15044754]

- van den Bogaart G, Meyenberg K, Diederichsen U, Jahn R, 2012 Phosphatidylinositol 4,5-Bisphosphate Increases Ca²⁺ Affinity of Synaptotagmin-1 by 40-fold. *J. Biol. Chem.* 287, 16447–16453. 10.1074/jbc.M112.343418 [PubMed: 22447935]
- Wang Z, Liu H, Gu Y, Chapman ER, 2011 Reconstituted synaptotagmin I mediates vesicle docking, priming, and fusion. *J. Cell Biol.* 195, 1159–1170. 10.1083/jcb.201104079 [PubMed: 22184197]
- Weber T, Zemelman BV, McNew JA, Westermann B, Gmachl M, Parlati F, Söllner TH, Rothman JE, 1998 SNAREpins: Minimal Machinery for Membrane Fusion. *Cell* 92, 759–772. 10.1016/S0092-8674(00)81404-X [PubMed: 9529252]
- Whittaker RG, Herrmann DN, Bansagi B, Hasan BAS, Lofra RM, Logigian EL, Sowden JE, Almodovar JL, Littleton JT, Zuchner S, Horvath R, Lochmüller H, 2015 Electrophysiologic features of *SYT2* mutations causing a treatable neuromuscular syndrome. *Neurology* 85, 1964–1971. 10.1212/WNL.0000000000002185 [PubMed: 26519543]
- Winn MD, Ballard CC, Cowtan KD, Dodson EJ, Emsley P, Evans PR, Keegan RM, Krissinel EB, Leslie AGW, McCoy A, McNicholas SJ, Murshudov GN, Pannu NS, Potterton EA, Powell HR, Read RJ, Vagin A, Wilson KS, 2011 Overview of the *CCP4* suite and current developments. *Acta Crystallogr. D Biol. Crystallogr.* 67, 235–242. 10.1107/S0907444910045749 [PubMed: 21460441]
- Winter G, 2010 *xia2*: an expert system for macromolecular crystallography data reduction. *J. Appl. Crystallogr.* 43, 186–190. 10.1107/S0021889809045701
- Winter G, Waterman DG, Parkhurst JM, Brewster AS, Gildea RJ, Gerstel M, Fuentes-Montero L, Vollmar M, Michels-Clark T, Young ID, Sauter NK, Evans G, 2018 *DIALS*: implementation and evaluation of a new integration package. *Acta Crystallogr. Sect. Struct. Biol.* 74, 85–97. 10.1107/S2059798317017235
- Wu D, Bacaj T, Morishita W, Goswami D, Arendt KL, Xu W, Chen L, Malenka RC, Südhof TC, 2017 Postsynaptic synaptotagmins mediate AMPA receptor exocytosis during LTP. *Nature* 544, 316–321. 10.1038/nature21720 [PubMed: 28355182]
- Zhang X-Y, La Russa VF, Reiser J, 2004 Transduction of Bone-Marrow-Derived Mesenchymal Stem Cells by Using Lentivirus Vectors Pseudotyped with Modified RD114 Envelope Glycoproteins. *J. Virol.* 78, 1219–1229. 10.1128/JVI.78.3.1219-1229.2004 [PubMed: 14722277]
- Zhou Q, Lai Y, Bacaj T, Zhao M, Lyubimov AY, Uervirojnangkoorn M, Zeldin OB, Brewster AS, Sauter NK, Cohen AE, Soltis SM, Alonso-Mori R, Chollet M, Lemke HT, Pfuetzner RA, Choi UB, Weis WI, Diao J, Südhof TC, Brunger AT, 2015 Architecture of the synaptotagmin–SNARE machinery for neuronal exocytosis. *Nature* 525, 62–67. 10.1038/nature14975 [PubMed: 26280336]

Highlights:

1. Graded, dominant-negative effects of disease-associated syt1 mutations
2. Clinical, physiological, and biochemical evidence for genotype-phenotype correlation
3. Functional segregation and positive allostery between the C2 domains of syt1
4. Rescue of mutant phenotypes by a clinically-approved drug in cultured neurons

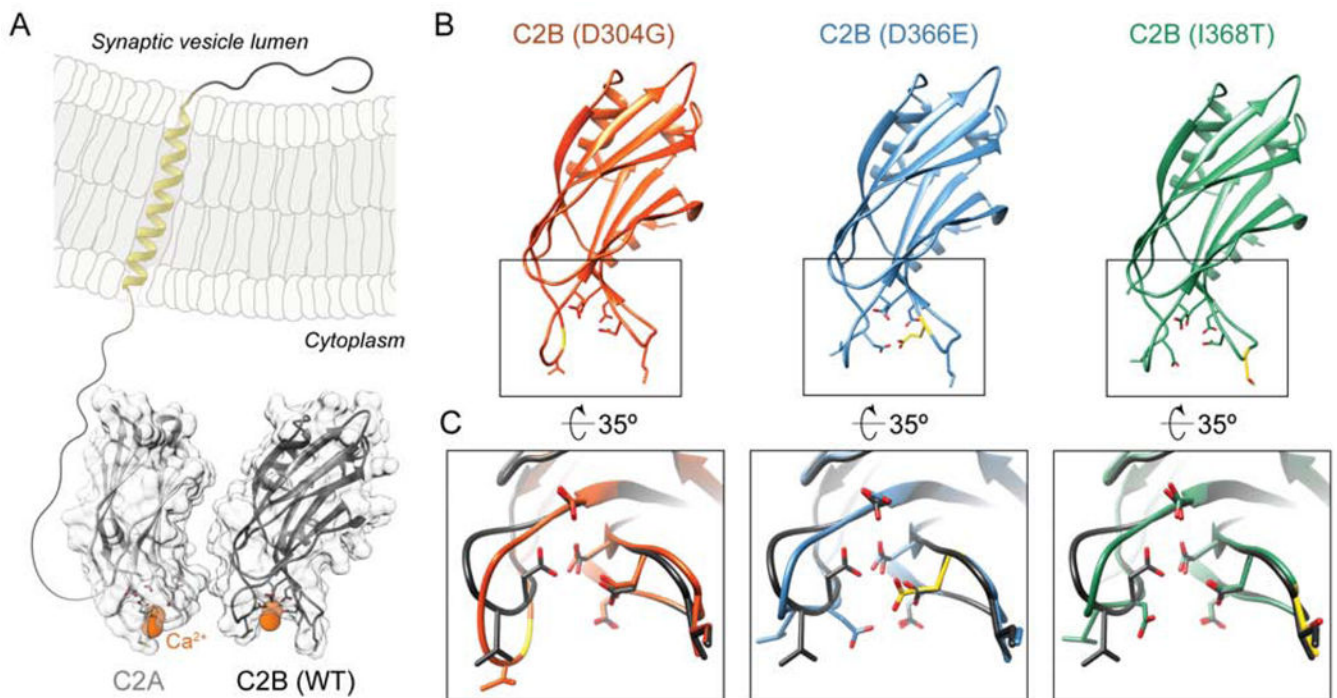


Figure 1. X-ray crystallographic structures of human syt1 C2B domains harboring disease-associated mutations.

(A) Schematic diagram of full-length syt1 embedded in a synaptic vesicle membrane. Each C2 domain was rendered from an X-ray crystal structure (C2A: PDB 1RSY, Sutton et al. 1995; C2B: 6TZ3, this work). The membrane is drawn to scale, and the N-terminal segments before C2A were added with a drawing program to illustrate the topology of syt1. Ca²⁺ ligands are rendered in wireframe, and Ca²⁺ ions are shown as orange spheres. (B) X-ray crystal structures of human syt1 C2B domains harboring disease-associated mutations. In each case, the overall fold of the WT C2 domain is preserved, and differences in the positions of Ca²⁺-binding/membrane-penetration loops are attributable to crystal packing. (C) Comparison of WT and mutant Ca²⁺-binding sites. The WT structure was rendered in grey and overlaid on each mutant to illustrate the effect of each mutation on the Ca²⁺-binding pocket: D304G removes an acidic Ca²⁺ ligand; D366E preserves the ligand but makes the binding pocket smaller; and I368T reduces the hydrophobicity of the membrane-penetrating tip of a Ca²⁺-binding loop.

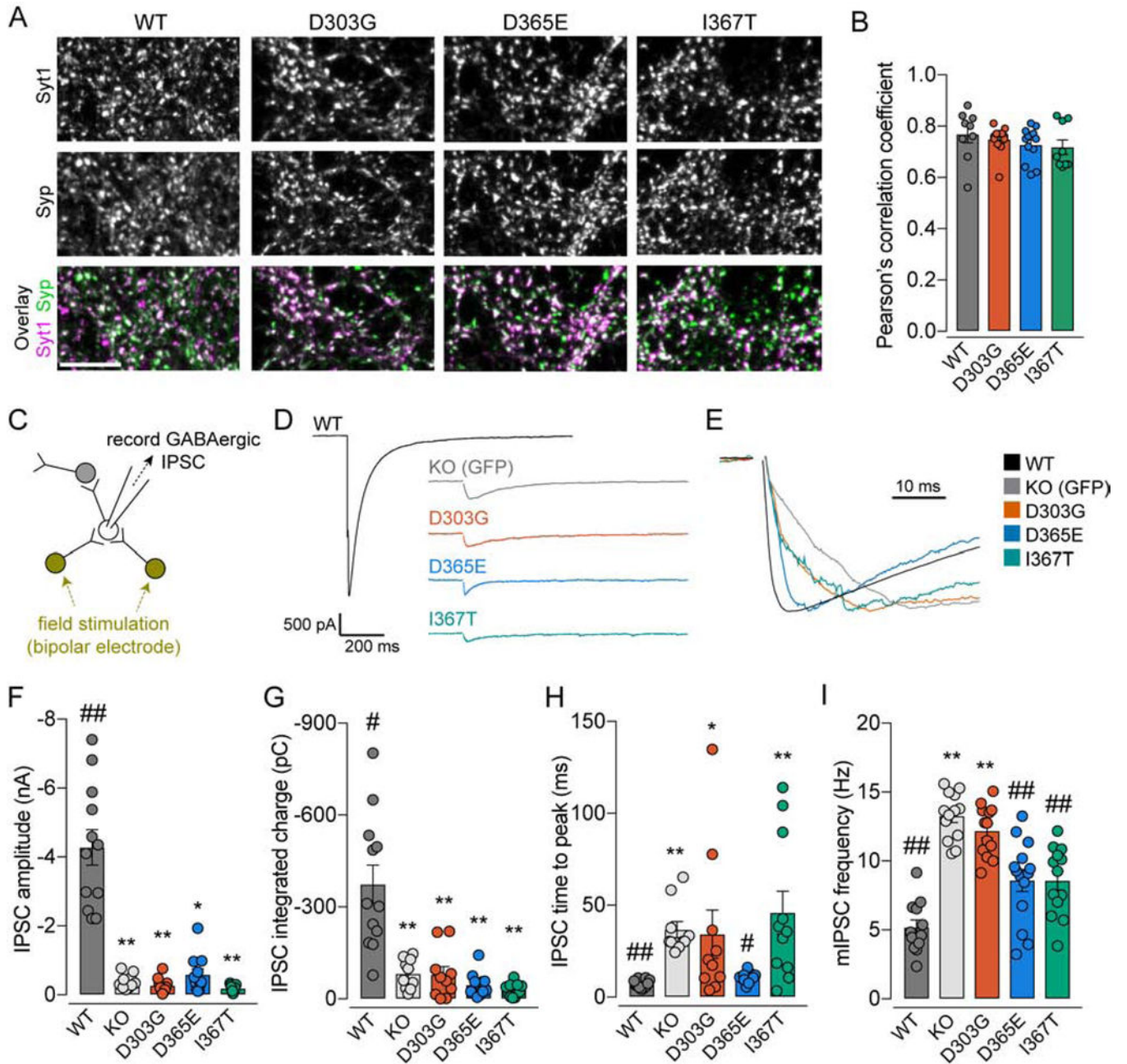


Figure 2. Disease-associated syt1 variants fail to support synaptic transmission but have distinct phenotypes.

In this and all subsequent figures, amino acid numbers corresponding to the murine protein are used. (A) Confocal micrographs of cultured hippocampal neurons expressing WT or mutant syt1 variants immunolabeled for syt1 and the presynaptic marker synaptophysin (syp). Scale bar, 10 μ m. (B) Colocalization of syt1 variants and syp was quantified via calculation of Pearson's correlation coefficient. No significant differences were observed between WT and mutant variants ($n = 9-12$ fields of view from 3-4 coverslips from at least 2 cultures). (C) Scheme of whole-cell patch clamp measurement of synaptic transmission in cultured neurons. (D) Average traces of evoked IPSCs from neurons expressing no syt1

(KO), WT, or mutant syt1 variants. Stimulus artifacts are removed from KO and mutant traces for clarity. (E) Evoked IPSCs shown with normalized amplitude on an expanded timescale. (F-H) Quantification of IPSC parameters. (I) Quantification of miniature IPSC frequency, recorded in TTX without stimulation. For panels D-I, $n = 10-15$ cells from at least 2 separate cultures. Significance values: *, $p < 0.05$ vs. WT; **, $p < 0.006$ against WT; #, $p < 0.05$ vs KO, ##, $p < 0.005$ vs KO (Kruskal-Wallis test with Dunn's multiple comparison test). See also Fig. S2.

Author Manuscript

Author Manuscript

Author Manuscript

Author Manuscript

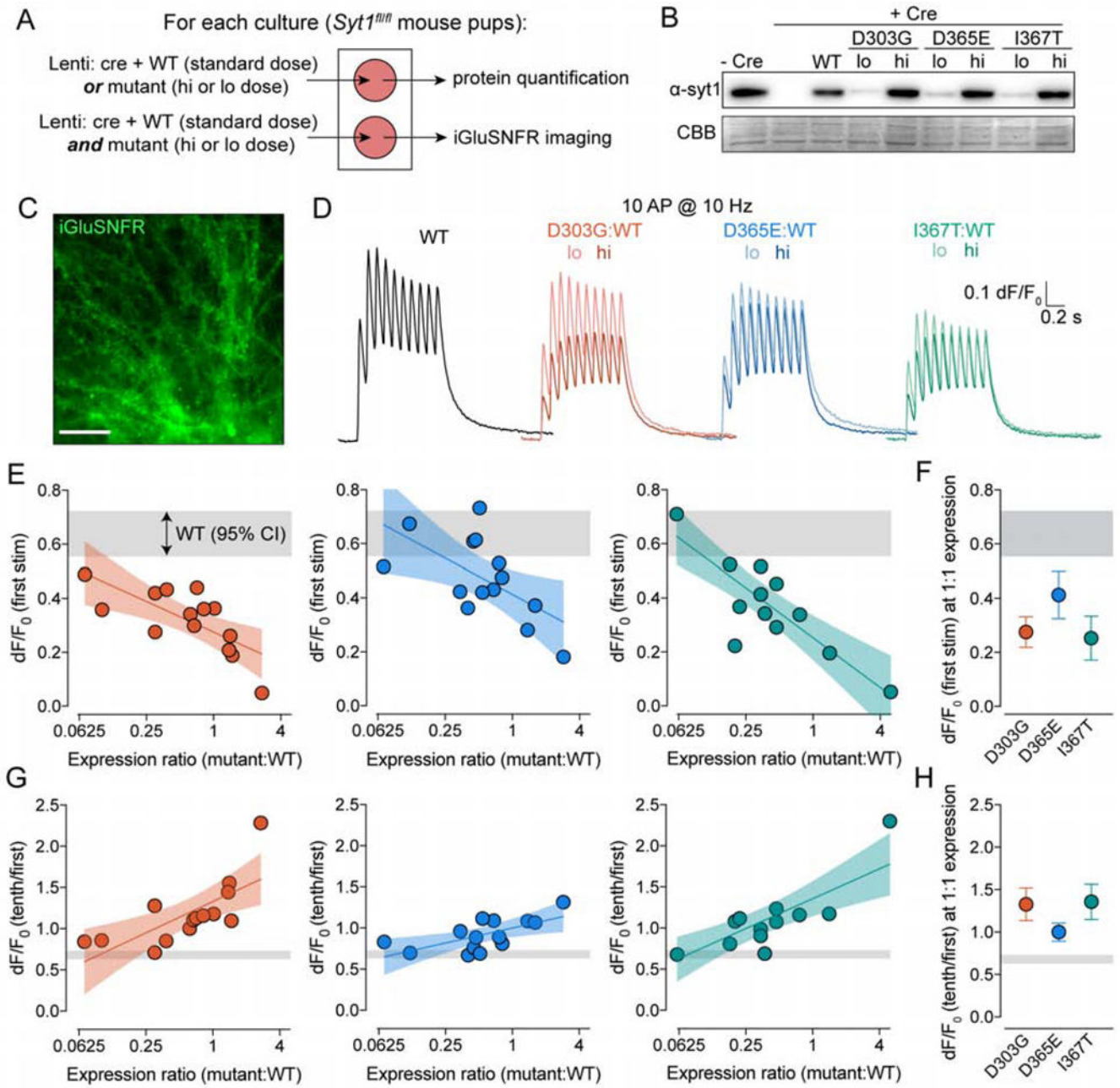


Figure 3. Co-expression of mutant and WT syt1 defines a dominant-negative action for each mutation that varies in potency.

(A) Scheme of approach used to address dominant-negative activity for each mutant. Quantification of expression level was performed in parallel with optical imaging of evoked neurotransmitter release. (B) Representative immunoblot and loading control (CBB: Coomassie Brilliant Blue) for syt1 quantification experiments. (C) Representative field of view for iGluSNFR imaging; scale bar, 25 μm. (D) Representative raw traces for iGluSNFR imaging of samples expressing only WT syt1 or WT syt1 in combination with mutant syt1. These traces correspond to the same experiment for which protein quantification is shown in panel (B). In each case, the same amount of lentivirus used to achieve the WT expression

shown in panel (B) was used, with either a low or high dose lentivirus encoding mutant *sytl* added simultaneously. (E) The normalized fluorescence transient (dF/F_0) upon the first stimulus pulse was plotted against the ratio of WT and mutant protein expressed using the same lentivirus dose in the same experiment. Each point represents an average of 4 fields of view from a single coverslip. Pooled results were plotted on a log-linear plot and fit by regression. Shaded regions depict 95% confidence intervals (CIs). (F) The 95% CIs corresponding to the log-linear model at 1:1 mutant:WT expression are plotted, demonstrating the increased dominant-negative potency of variants D303G and I367T over D365E. (G) As in panel (E), but for the amplitude of the tenth fluorescence transient normalized to the first fluorescent transient ($dF/F_0(\text{tenth/first})$). (H) as in panel (F), but with 95% CI of the fit to $dF/F_0(\text{tenth/first})$ at 1:1 mutant:WT expression plotted. For all experiments, $n = 13\text{--}14$ coverslips from at least 4 separate cultures. See also Figs. S3, S4 and Table S2.

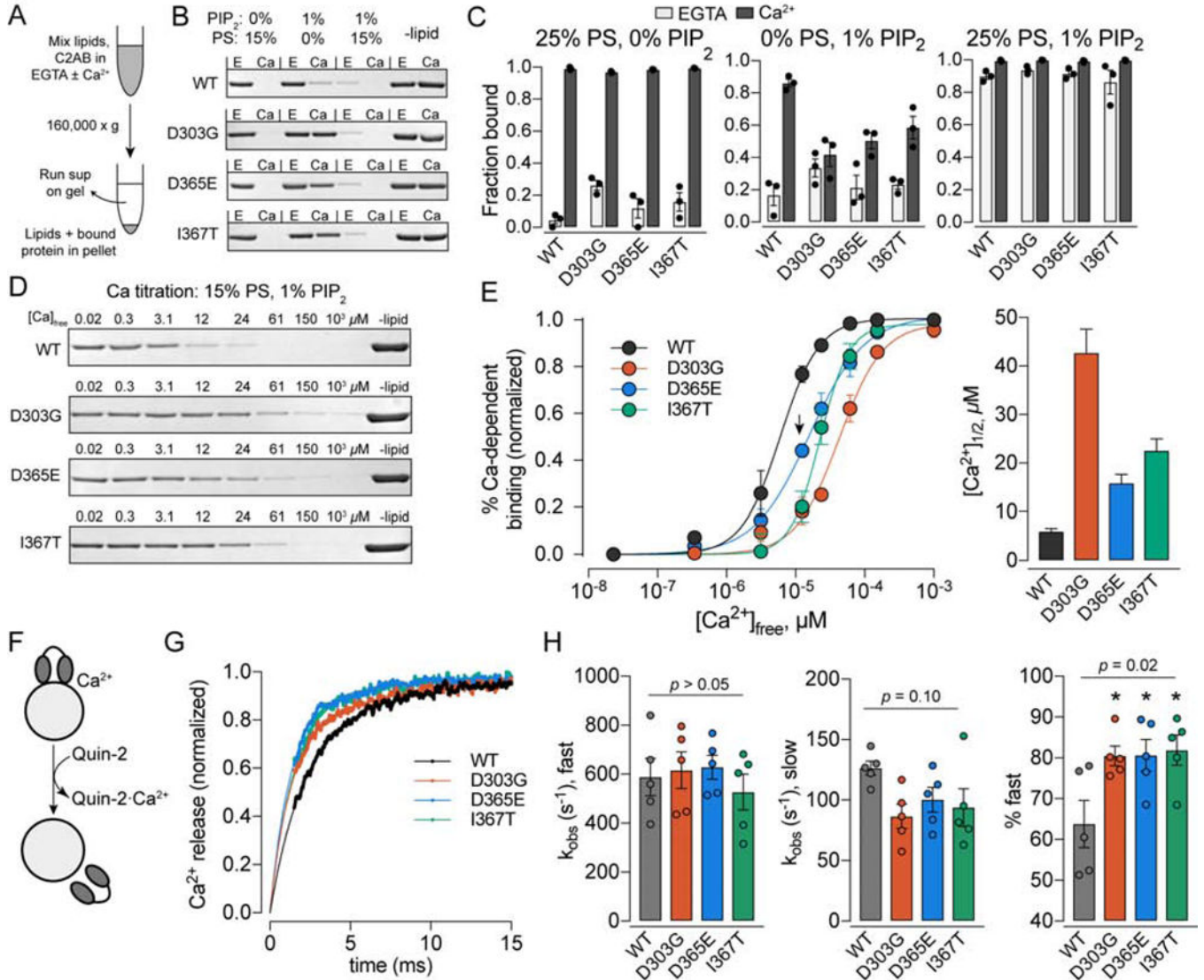


Figure 4. Disease-associated syt1 variants cause deficits in Ca²⁺-dependent lipid binding activity.

(A) Scheme of the cosedimentation assay used to monitor lipid binding. (B) Representative Coomassie-stained gel showing depletion of protein from supernatant upon binding to liposomes. (C) Pooled results using the indicated lipid compositions ($n = 3$ independent experiments). (D) Representative Coomassie-stained gel of a cosedimentation performed while titrating $[Ca^{2+}]_{free}$. (E) Pooled results of Ca²⁺ titration cosedimentations ($n = 3-4$ independent experiments). Dose-response curves were fit using the Hill equation; error bars represent standard error. Calculated Hill coefficients are noted in the main text. Arrow indicates a point at which D365E displayed enhanced binding *versus* I367T ($p < 0.03$, Mann-Whitney test). (F) Assay scheme for measuring the kinetics of Ca²⁺ release from protein-membrane complexes. Ca²⁺, syt1 C2AB, and liposomes are combined, then rapidly mixed with the fluorescent Ca²⁺ indicator Quin-2. (G) Average traces for Ca²⁺ release kinetics; these were fit with double exponential functions (smooth lines) extrapolated to $t = 0$. (H) Parameters from the biexponential fits are plotted. Each mutation had minor effects on

the slow component of Ca^{2+} release but also increased the relative amplitude of the fast component of Ca^{2+} release ($n = 5$ independent experiments). Significance values: indicated p -values indicate results of one-way ANOVA; *, $p < 0.05$ vs. WT, Dunnett's multiple comparisons test. See also Figs. S5, S6.

Author Manuscript

Author Manuscript

Author Manuscript

Author Manuscript

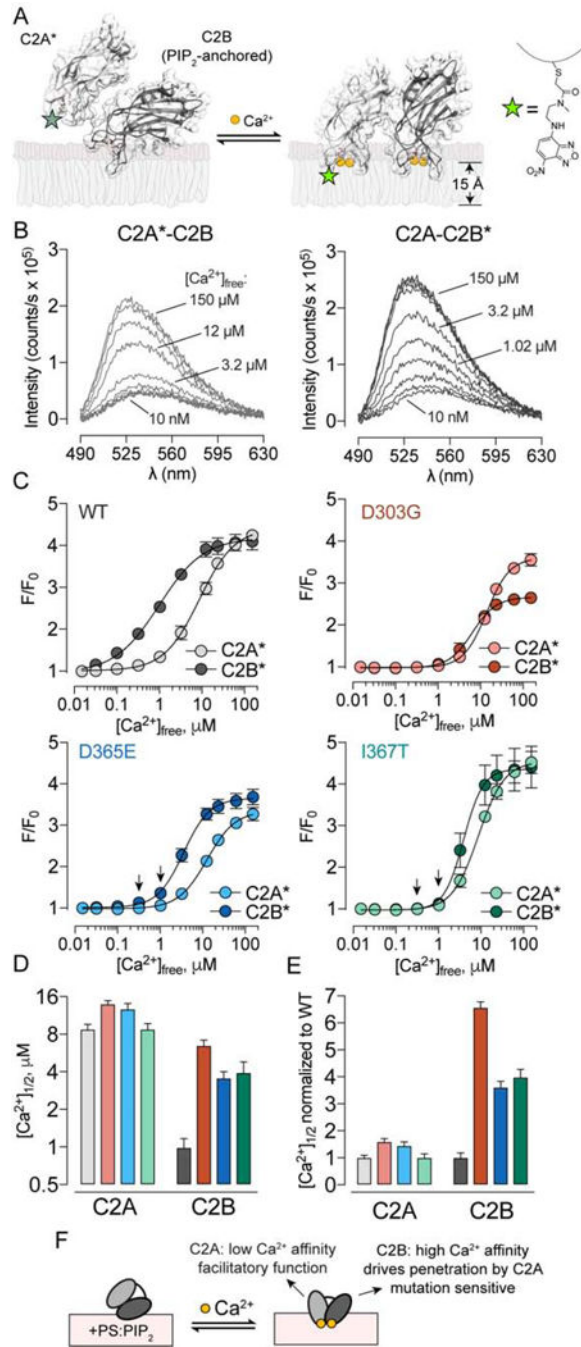


Figure 5. Disease-associated syt1 variants disrupt a low Ca^{2+} affinity membrane penetration mode in C2A and a novel, high Ca^{2+} affinity penetration mode in C2B.

(A) Scheme illustrating the membrane penetration assay, with insertion depths depicted according to measurements of WT syt1 in Bradberry et al. (2019). Syt1 C2AB was labeled on C2A or C2B with NBD (green star) and fully adsorbed to liposomes containing 15% PS and 3% PIP_2 before the addition of Ca^{2+} . (B) Representative traces of NBD fluorescence emission from WT C2AB upon titration of Ca^{2+} . (C) NBD fluorescence was plotted against $[\text{Ca}^{2+}]_{\text{free}}$ ($n = 4$ unique combinations of lipid and protein batches) for WT and mutant syt1. Overlaid lines represent fits using the Hill equation (Hill coefficients noted in main text).

Arrows indicate points at which F/F_0 was significantly higher for D365E vs. I367T ($p < 0.03$, Mann-Whitney test). (D) $[Ca^{2+}]_{1/2}$ values for penetration by C2A and C2B for WT and mutant variants. Error bars represent standard errors. (E) $[Ca^{2+}]_{1/2}$ values for penetration normalized to WT. Error bars represent propagated standard errors. (F) Model depicting specialization of the individual C2 domains of syt1. See also Fig. S7.

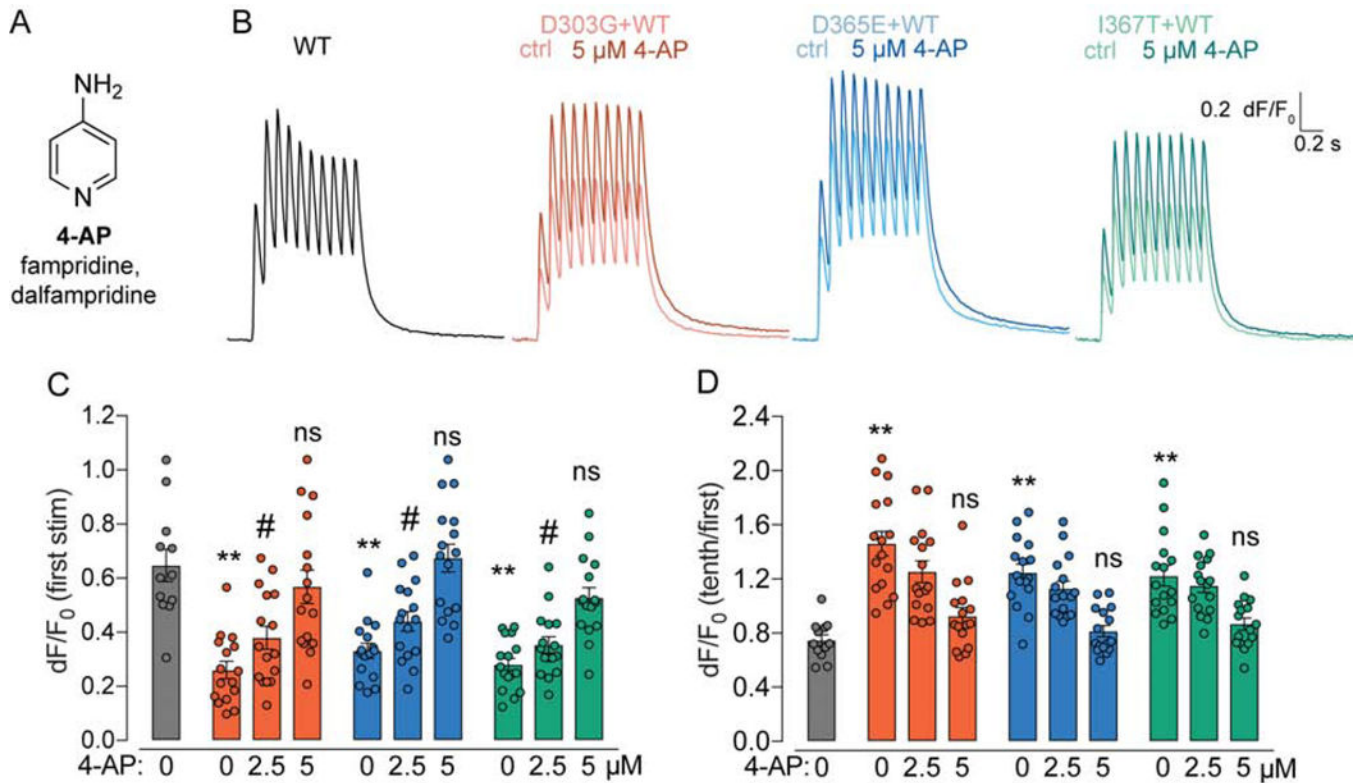


Figure 6. Rescue of dominant-negative syt1 mutant phenotypes by a clinically approved, centrally acting K⁺ channel blocker.

(A) Structure and generic names of 4-aminopyridine, a centrally-acting voltage-gated K⁺ channel antagonist clinically approved for the treatment of multiple sclerosis. (B) Representative iGluSnFR dF/F₀ traces before and after application of 5 μ M 4-aminopyridine. Cultures were transduced with lentivirus to achieve ~1:1 expression of mutant and WT protein. (C) dF/F₀ transients upon the first stimulation of a 10-AP train are plotted for each genotype in control bath, followed by the addition of 4-AP to 2.5 and 5 μ M. The same fields of view were imaged in control and each 4-AP condition. (D) as in (C) but for dF/F₀ (tenth/first). Both synaptic release parameters normalized in response to 4-AP in a dose-dependent fashion, with near-complete rescue of WT glutamate release at 5 μ M 4-AP. For all experiments, $n = 12$ –16 fields of view from 3–4 coverslips from at least 2 separate cultures. Significance values: **, $p < 0.0001$ vs WT; ns, $p > 0.3$ vs. WT (One-way ANOVA with Dunnett's multiple comparisons test); #, $p < 0.01$ vs ctrl for the same genotype (paired t -test).

Table 1.
Clinical histories of patients with *de novo* heterozygous missense mutation in *SYT1*.

Histories were obtained directly from patient records and interviews with family members (D304G, D366E) or from previously published case histories (I368T). Phenotypes associated with these mutations are highly variable; among these patients, mutation D365E is associated with a substantially milder phenotype.

	D304G (male)	D366E (female)	I368T (male)
Infantile hypotonia	Yes	Yes	Yes
First sat independently	3 yrs	14 mo.	4 yrs
First walked	-	2 yrs	10 yrs
Self-injurious behavior	Yes	No	Yes
Movement disorder	Yes: dystonia	No	Yes: dystonia, ballismus of lower limbs, chorea
Receptive language	None	Responds to name	None
Expressive language	None	4–5 words at age 4 yrs	None
MRI brain	Normal	Normal	Normal
Epilepsy	No	No	No
EEG	(at 4 yrs, asleep) High-amplitude slow waves with intermittent epileptiform spikes	(at 2 yrs, awake) Diffuse slow background rhythm with frequent high-voltage (180–240 μ V) slow waves	(at 2 yrs, awake) Diffuse slow background rhythm, frequent very-high amplitude (300–600 μ V) slow waves
Visual Evoked Potentials	Not assessed	Increased latency, reduced amplitude	Increased latency, reduced amplitude
Other conditions	Scoliosis, gastroesophageal reflux, esotropia	Atrial septal defect, laryngomalacia, esotropia	Talipes equinovarus, esotropia

Table 2.

Summary of clinical, physiological, and biophysical effects of disease-associated syt1 mutations.

	D304G	D366E	I368T
Clinical severity *	Severe	Mild to moderate	Moderate to severe
Evoked synaptic transmission	Minimal	Minimal with kinetic rescue	Minimal
Clamping of spontaneous synaptic transmission	Minimal	Some	Some
Dominant-negative potency	High	Low	High
Impairment of Ca²⁺-dependent membrane binding	Severe	Moderate(-)	Moderate(+)
Impairment of Ca²⁺-dependent membrane penetration	Severe	Moderate(-)	Moderate(+)

* Including those cases reported in Baker et al., 2018.

Author Manuscript

Author Manuscript

Author Manuscript

Author Manuscript

KEY RESOURCES TABLE

REAGENT or RESOURCE	SOURCE	IDENTIFIER
Antibodies		
mAb 48 (ASV 48)	Iowa DSHB	Cat# mAb 48 (asv 48); RRID AB_2199314
Guinea pig anti-synaptophysin rabbit pAb	Synaptic Systems	Cat# 101 004; RRID AB_1210382
Goat anti-mouse IgG2b HRP-conjugated secondary	Thermo Fisher	Cat# PA1-84710; RRID AB_933958
Goat anti-guinea pig IgG pAb, Alexa488-conjugated	Thermo Fisher	Cat# A-11073; RRID AB_2534117
Goat anti-mouse IgG2b pAb, Alexa647-conjugated	Thermo Fisher	Cat# A-21242; RRID AB_2535811
Bacterial and Virus Strains		
BL21(DE3) <i>E. coli</i>	Thermo Fisher	Cat# C600003
Biological Samples		
Saliva from patients	Study participants	N/A
Chemicals, Peptides, and Recombinant Proteins		
Prep-It L2P	DNA Genotek	Cat# PT-L2P-1.5
Coomassie Brilliant Blue	Bio-Rad	Cat# 161-0406
Thrombin	Sigma	Cat# T4648
CNQX disodium salt	Tocris	Cat# 1045
D-APV	Tocris	Cat# 0106
Picrotoxin	Tocris	Cat# 1128
4-AP	Sigma	Cat# 275875
QX314 chloride	Tocris	Cat# 2313
POPC	Avanti Polar Lipids	Cat# 850457
POPS	Avanti Polar Lipids	Cat# 840034
POPE	Avanti Polar Lipids	Cat# 850757
Liver PI	Avanti Polar Lipids	Cat# 840042
Brain PIP ₂	Avanti Polar Lipids	Cat# 840046
Cholesterol	Avanti Polar Lipids	Cat# 700000
Quin-2	Sigma	Cat# 08520
IANBD amide	Thermo Fisher	Cat# D2004
HaloLink beads	Promega	Cat# G1915
Hibernate-A	BrainBits	Cat# HA
Trypsin-EDTA	Corning	Cat# 25-053-CI
Poly-D-lysine HBr	Sigma	Cat# P0899
Neurobasal-A medium	Gibco	Cat# 10888-022

REAGENT or RESOURCE	SOURCE	IDENTIFIER
B27	Thermo Fisher	Cat# 17504044
GlutaMAX	Gibco	Cat# 35050061
Protease inhibitor tablets	Sigma (Roche)	Cat# 11936170001
Critical Commercial Assays		
ORACollect for pediatrics DNA collection kit	DNA Genotek	Cat# OC-175
Experimental Models: Cell Lines		
HEK293T (used for virus production)	ATCC	Cat# CRL-3216
Experimental Models: Organisms/Strains		
Mouse: <i>SYT1</i> ^{+/+} ; B6;Syt1 ^{tm1Sud/J}	The Jackson Laboratory	Stock# 002478
Mouse: <i>SYT1</i> ^{fl/fl} ; B6;Syt1 ^{fl/fl} /J	Quadros et al. 2017	N/A
Oligonucleotides		
GCAAGAGAAATTGGGTGATATCTGCTTCTCCC (<i>SYT1</i> exon 6 forward primer)	This work	N/A
CGCAGCATGTGCCCATGC (<i>SYT1</i> exon 6 reverse primer)	This work	N/A
GGGCCTTATCTCTAGAGCTAGATGATTCATATTCATTCATGGC (<i>SYT1</i> exon 8 forward primer)	This work	N/A
CTTCTTGACGGCCAGCATGGCATC (<i>SYT1</i> exon 8 reverse primer)	This work	N/A
Recombinant DNA		
Plasmids: His ₆ -MBP-Syt1 WT and mutants for crystallization (backbone: pET)	This study	N/A
Plasmids: GST-Syt1 WT and mutants for lipid and Ca ²⁺ binding studies (backbone: pGEX-4T)	This study	N/A
Plasmids: Syt1 WT and mutants IRES mRuby3 for lentiviral preparation and transduction (backbone: pFUGW with human synapsin promoter)	This study	N/A
Plasmid: iGluSNFR (backbone: FUGW with CaMKIIa promoter)	This study	N/A
Plasmid: pLenti-hSynapsin-Cre-WPRE	Sakurai et al. 2016	Cat# 86641
Plasmid: pLTR-G	Reiser et al. 1996	Cat# 17532
Plasmid: pCD/NL-BH*	Zhang et al. 2004	Cat# 17531
Plasmid: FUGW	Lois et al. 2002	Cat# 14883
Plasmid: GFP for lentiviral expression (backbone: FUGW with human synapsin promoter)	This paper	N/A
Plasmids: His ₆ -HaloTag-Syt1 WT and mutants for SNARE binding assays (backbone: pTrcHis)	This paper	N/A
Plasmid: His ₆ -SNAP25B:Syntaxin1A heterodimer (backbone: pRSF Duet)	This paper	N/A
Software and Algorithms		
Micro-manager	Edelstein et al. 2010	https://micro-manager.org/
FIJI	Schindelin et al. 2012	https://fiji.sc/
RStudio	RStudio, inc	https://rstudio.com/
GraphPad Prism	GraphPad, inc	https://www.graphpad.com/scientific-software/prism/

REAGENT or RESOURCE	SOURCE	IDENTIFIER
pClamp	Molecular Devices	https://www.moleculardevices.com/products/axon-patch-clamp-system/acquisition-and-analysis-software/pclamp-software-suite

Author Manuscript

Author Manuscript

Author Manuscript

Author Manuscript